Fonseca et al. (2026)
The case for metal saturation in the lunar mantle
Advances in Geochemistry and Cosmochemistry 2(1): 754, https://doi.org/10.33063/agc.v2i1.754

Research article

The case for metal saturation in the lunar mantle

Raúl O. C. Fonseca[1] ✉ Christopher Beyer[1] Stephan Schuth[1] Felipe P. Leitzke[2]

[1] Institut für Geologie, Mineralogie und Geophysik, Ruhr-Universität Bochum, Germany
[2] Universidade Federal de Pelotas, Rio Grande do Sul, Brazil

✉ **Correspondence to:** Raúl O. C. Fonseca: raul.fonseca@rub.de

Author contributions: Conceptualization: ROCF, FPL; Formal Analysis: ROCF, FPL; Investigation: ROCF, CB, SS; Writing – original draft: ROCF, CB, SS; Writing – review & editing: ROCF, CB, SS.

Data, code, and outputs: Fonseca et al. (2026) https://doi.org/10.5281/zenodo.20525326

Submitted: 2025-03-05
Accepted: 2026-03-24
Published: 2026-06-29

Production editor:
Ananya Mallik

Handling editor:
Romain Tartèse

Reviews:
Two anonymous reviewers

Copyediting:
Elliot Carter,
Marthe Klöcking

Lunar basalts are more reduced than their terrestrial counterparts, often containing native metal, suggesting a similarly reduced, possibly metal-saturated lunar mantle. However, whether determined oxygen fugacities (fO_2) accurately reflect mantle conditions remains debated. Processes like H-implantation and CO-degassing during eruption may locally reduce samples, leading to underestimation of fO_2 and implying more oxidizing mantle conditions than sample chemistries would suggest. Additionally, correlations between siderophile and chalcophile elements (e.g., W, Cu) and incompatible elements (e.g., U, Yb) seemingly contradict metal presence in mare basalt sources. Yet, the median lunar interior fO_2 suggests residual Fe-bearing metal stabilization during mantle melting. We review evidence for and against residual metal in the lunar mantle and its implications. Equilibrium thermodynamics supports metal saturation at fO_2 levels of IW −1 or lower if metal contains ∼10 wt% S. To test this, we conducted experiments at ∼1500 °C and 1.5 GPa on highly siderophile elements (Pt, Pd, Rh, Os, Ir, Re), W, and Mo, as well as an experiment at 4.5 GPa and 1900 °C to simulate lunar core-lunar magma ocean equilibrium. Our results show that the low siderophile element abundances in mare basalts are consistent with partial melting of a lunar mantle both saturated in ∼0.1 wt% Fe-Ni-S metallic melt and previously depleted in siderophile elements due to core formation.

1 Introduction

After the first samples were brought back from the Apollo lunar landing missions, one of their most surprising and idiosyncratic features was the fact that they often contained native Fe-metal. The presence of Fe-metal in lunar samples presumably places oxygen fugacity (fO_2) during mare basalt crystallization below the Fe-FeO (IW) redox buffer, in direct contrast to the vast majority of terrestrial magmatic rocks, which typically result from partial melting at redox conditions up to 100,000 times more oxidized (cf. Wadhwa, 2008). The presence of native metal in lunar samples, coupled with their overall depletion in siderophile (i.e. iron loving) elements, led early researchers to conclude that lunar mantle sources must themselves be metal-saturated (Wolf and Anders, 1980; Newsom, 1986). However, this possibility has been the subject of much debate. For example, several secondary processes have been invoked to explain the presence of metal in lunar samples, including local reduction due to H implantation by solar wind (DesMarais et al., 1974; Taylor et al., 2004), and via the degassing of carbon and sulfur during mare basalt eruption (Sato, 1978). For example, Taylor et al. (2004) have shown that solar wind implantation of hydrogen into a high-Al basalt sample recovered during the Apollo 14 mission (14053), has resulted in "extreme reduction". Such evidence of local reduction includes the conversion of fayalite into tridymite plus native metal, and the identification of exsolution lamellae of ilmenite in ülvospinel. Sato (1978) pointed out that a redox exchange between C and Fe species in lunar samples leads to a reduction in fO_2 during lunar volcanism until it is buffered by the presence of Fe metal, following redox exchanges like those seen below:

$$\mathrm{FeO} + \mathrm{C} = \mathrm{Fe} + \mathrm{CO} \quad (1)$$

$$2\,\mathrm{FeO} + \mathrm{C} = 2\,\mathrm{Fe} + \mathrm{CO_2} \quad (2)$$

Indeed, lunar samples have been shown to contain 40–300 µg g^{-1} of C (Moore and Schilling, 1973; Moore et al., 1973; Wetzel et al., 2015), the degassing of which could have led to the reduction of lunar lavas. Recently, Day (2018) waded into this debate by pointing out that silicate melts produced via partial melting of metal- or

sulfide-saturated lunar mantle sources would be expected to develop supra-chondritic Re/Os, due to differences in the metal/silicate or sulfide/silicate partition coefficients for both elements. Consequently, lunar mare basalts should have developed radiogenic and suprachondritic $^{187}Os/^{188}Os$. However, the most primitive high-MgO mare basalts have chondritic relative abundances of the HSE, and measured $^{187}Os/^{188}Os$ falls within the range seen in chondrites (0.1265 to 0.1345; Day et al., 2007; Day and Walker, 2015). Day (2018) also argued that the presence of residual metal and sulfide in lunar mantle sources should have resulted measurable fractionations between siderophile and chalcophile elements like W and Cu and similarly incompatible lithophile elements like U, Th and Yb. However, Day (2018) noted that these elements correlate similarly in lunar basalts as they do in terrestrial oceanic basalts (Fig. 1). This led Day (2018) to conclude that the lunar mantle is unlikely to be metal- or sulfide-saturated, and that the presence of metal in some lunar basalts is incidental and likely the result of secondary and localized reduction processes, and/or the assimilation of reduced regolith by lunar basalts. Moreover, Steenstra et al. (2018) and Ding et al. (2018), based on the experimental determination of the sulfur content at sulfide saturation (SCSS) of synthetic mare basalts, and in the case of the former also Ni and Co systematics of mare basalts, have suggested that the lunar mantle is unlikely to be saturated in a sulfide liquid (i.e. molar Fe/S ~1). They reached this conclusion because sulfur contents of undegassed melt inclusions in mare basalt olivines are lower than their determined SCSS, indicating lunar mantle sources could not have been saturated in a sulfide phase.

The potential presence or absence of residual metal in lunar mantle sources has obvious implications to our interpretation of siderophile element systematics in lunar basalts. Even though the presence of metal in lunar mantle sources is consistent with the overall observation that lunar mare basalts are siderophile element depleted (Wolf and Anders, 1980; Newsom, 1986), the issues raised by Day (2018), Ding et al. (2018), Steenstra et al. (2018) and others have merit and need sober examination. The aim of this manuscript is to address four key questions: 1) Are the fO_2 derived from lunar basalts representative of their sources? 2) If so, are these fO_2 compatible with the notion that lunar mantle sources are metal-saturated? 3) What sort of compositions would one expect this residual metal to have? 4) What are the implications of the presence of residual metal in lunar mantle sources? To address these questions, we will outline the case for residual metal in the lunar mantle. Assuming its presence, we conducted experiments investigating the partitioning behavior of Mo, W, Ru, Os, Ir, Rh, Pt, Pd, and Re between metal and a synthetic low-Ti mare basalt modeled after low Ti basalt 12005 (Dungan and Brown, 1977). Our goal was to generate partitioning data relevant to lunar mare basalt petrogenesis. These data inform our models on whether the presence of residual metal in lunar mantle sources aligns with present-day siderophile element abundances observed in primitive low-Ti mare basalts.

2 Arguments for and against the presence of metal in lunar mantle sources

As mentioned, the notion of widespread Fe-metal saturation in the lunar mantle raises several important concerns (Day, 2018) but there is also plenty of evidence that support the possibility that the lunar mantle is to some extent metal-saturated, as recorded in geochemical features of lunar mare basalts. One factor to consider, is that secondary reduction processes identified in lunar samples may not be as pervasive as previously thought. For example, Taylor et al. (2004), in their study of the ultra-reduced Apollo 14 high-Al basalt mentioned above, noted that the extreme reduction seen in this sample is largely restricted to the mesostasis found in the outermost part of this 250 g sample. Indeed, solar wind implantation appears to be superficial at best (first 100 nm) and sees large diurnal variations, especially around lunar equatorial regions where most mare basalt samples have been recovered (Farrell et al., 2015). This means that the wholesale reduction of a mare basalt via the assimilation of regolith that sustained H-implantation is likely limited due to the small amount reduced material being assimilated. Also, Taylor et al. (2004) pointed out that the Fe metal seen in sample 14053 does not have the appearance of primary native Fe metal found in other lunar mare basalt samples, which typically occur as roundish grains (cf. Dickey Jr, 1970; Dungan and Brown, 1977; Day and Paquet, 2021), and are thus likely to consist of primary phases. On the issue of reduction by C degassing (i.e. CO), C has such a large reduction capacity (Equations 1 and 2) that the reduction of small amounts of FeO, Cr_2O_3 and TiO_2 by C produces CO gas in high enough abundance to drive the pyroclastic eruptions in the lunar surface (see Rutherford et al., 2017, and references therein). This reduction process is thus not anticipated to result in a dramatic shift in the redox condition of the original magma (Wadhwa, 2008), mainly because the amount of C available is too small to reduce a high enough proportion of very abundant FeO in primitive lunar melts (cf. Wetzel et al., 2015). Moreover, Sato (1978) also noted that H-degassing of lunar samples would drive their relative fO_2 to higher values, offsetting somewhat the prior reduction by C. Likewise, degassing of sulfur will either oxidize or reduce a silicate melt, depending on the dominant sulfur gas species (i.e. H_2S or SO_2; Métrich et al., 2009). During lunar magmatism, where reduced S species are expected to dominate, even though only minor S-degassing is expected (Gaillard et al., 2011), H_2S degassing would lead to the oxidation of the magma (Métrich et al., 2009). Note that we are not arguing that degassing-related reduction processes have not affected lunar basalt samples samples, but rather that they probably are not able to dramatically shift the fO_2 associated with the formation of lunar mare basalts (Wadhwa, 2008).

Day (2018) also pointed out that the chondritic Os isotopic composition of primitive low-Ti mare basalts and

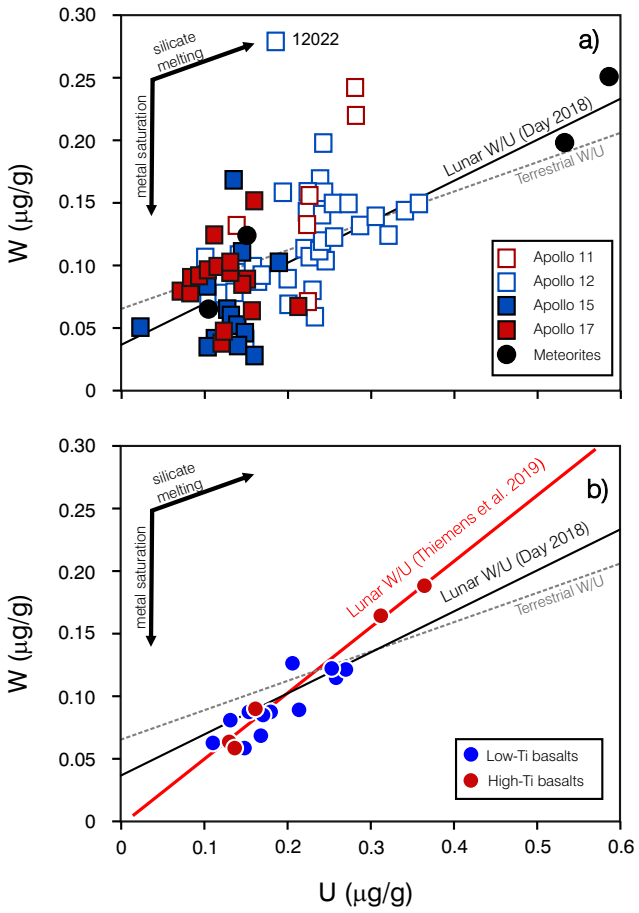

Figure 1. Correlation between W and U in lunar samples. (a) Correlation of W and U using data from lunar meteorites (black circles; Day, 2018), superimposed with W and U data from the lunar sample compendium (figure modified after Day, 2018). (b) Correlation between W and U using high-precision isotope dilution data from Thiemens et al. (2019) compared to similar correlations using data from Day (2018) for lunar and terrestrial W/U. Note that the lunar W/U reference line, as constrained by the dataset of Thiemens et al. (2019), is clearly more fractionated compared to both the terrestrial reference line and that constrained by the lunar data from Day (2018).

their broadly chondritic HSE values are inconsistent with metal-saturation in their sources. However, the Os isotope composition of the basalts can be easily explained by assimilation of lunar regolith that has experienced meteoritic contamination (Brenan et al., 2019). Assimilation of less than 1 % of HSE-rich lunar regolith by a lunar basalt will not affect the abundances of moderately siderophile elements like Ni, Co and W, but it will undoubtedly lead to a large increase in its HSE concentrations. Regolith assimilation will also introduce a chondritic Os isotope composition to the erstwhile Os-depleted mare basalts (cf. Brenan et al., 2019). As such, the argument that the chondritic HSE abundances and Os isotope composition of mare basalts is inconsistent with metal-saturation in lunar mantle sources is perhaps flawed. There is also evidence for the fractionation of W and Mo from U and Th in the lunar mantle. Several studies have pointed out that W is more compatible than U and Th during lunar mantle melting (Palme and Rammensee, 1982; Palme and Wänke, 1975). Day (2018) questioned this conclusion by pointing out that W and U are similarly correlated in primitive unfractionated lunar basalts as they are for terrestrial oceanic basalts (Figure 1a). However, Day (2018) did not use the bulk of data from the lunar sample compendium in their comparison, and a more thorough examination of such data reveals not only much scatter, but also some evidence of W depletion relative to U, as would be expected if partial melting took place under metal-saturated conditions. This point is reinforced by Thiemens et al. (2019), who based on high-precision isotope dilution data, noted that mare basalts display fractionated U/W and Th/W compared to terrestrial basalts (Figure 1b), which they concluded was likely due to W being retained in lunar mantle sources relative to U and Th. Moreover, Fonseca et al. (2014) and Leitzke et al. (2016), based on their experimental mineral/melt partitioning data, noted that W behaves slightly more compatible than U and Th under the reducing conditions (around IW −1) thought to be prevalent during lunar mantle melting. When these authors combined their experimental datasets with trace element data from the lunar sample compendium, they could reproduce lunar trends in U/W (and U/Th) vs. Hf/W space. To do this, Fonseca et al. (2014) and Leitzke et al. (2016) assumed partial melting of lunar mantle cumulates under reducing conditions (between IW −1 and IW −1.5), and in the case of high-Ti basalts with partial melting in the presence of residual metal and ilmenite. The Mo/W ratio of lunar basalts (~0.1; Newson, 1995; O'Neill, 1991) is much lower than that of terrestrial basalts (BSE ~ 2.4; Palme and O'Neill, 2014; Liang et al., 2017). Based on experimental partitioning data, Leitzke et al. (2017) proposed that Mo is more compatible than W during partial melting of the lunar mantle. This is attributed to two factors: the presence of residual metal in the mantle source and the predominance of the more compatible Mo^{4+} oxidation state under lunar conditions, in contrast to the more incompatible Mo^{6+} species prevalent in terrestrial magmatism (e.g., Holzheid et al., 1994; Danielson et al., 2011). Leitzke et al. (2017) obtained the best fit to natural Mo/Hf vs. Hf/W data using model basalt compositions generated by partial fractional melting of lunar mantle cumulates – originally crystallized from a BSE-like lunar magma ocean – under reducing conditions (IW −1.5) and in the presence of residual metal.

It is important to note that the notion implying that residual metal during partial melting would automatically make W behave like a compatible element is perhaps a misconception. Tungsten has overall lower metal/silicate-melt partition coefficients (literature values range between 7–100 with a mode of 30) compared to elements like Mo (ca. 200–300, see compilation by Rai and van Westrenen, 2014). The issue becomes exacerbated when the metal phase includes lighter elements like S or C in it, which drives $D_W^{metal/melt}$ to even lower values (cf. Wade et al., 2012; Steenstra et al., 2017). In terms of mass balance, residual metal, if present in lunar mantle sources, has a much smaller

contribution to the bulk partitioning behavior of W during partial melting when compared to silicates. This, coupled with the fact that W is highly incompatible in all mantle silicates and oxides ($D_W^{mineral/melt}$ between 10^{-3} and 10^{-5}; see Adam and Green, 2006; Fonseca et al., 2014; Leitzke et al., 2016, 2017) means that the bulk partitioning behavior of W during lunar mantle melting is still that of an incompatible element, albeit to a lesser extent when compared to partial melting of Earth's mantle. This explains why W is still correlated with traditionally incompatible elements like U, Th, and La in lunar samples (Palme and Wänke, 1975), even if ratios between these elements appear to be more fractionated than in their terrestrial counterparts. A similar argument was made by Brenan et al. (2019), who pointed out that small amounts of metal and/or sulfide in lunar mantle sources would only be expected to impact those elements that are very chalcophile and/or siderophile, like the highly siderophile elements (HSE).

Several other characteristics of lunar basalts support the assertion that their mantle sources are reduced and may be metal-saturated. For example, the low Ni and Cr abundances of lunar basalts indicate that mantle melting took place at reducing conditions, between IW −1 and IW −2 (Jones, 2004; Delano, 1990). Similarly, Steele et al. (1992), in their study of Apollo 15 green glasses, proposed an oxygen fugacity for these glasses of ∼IW −2, based on the Ni and Co content of these glasses. Indeed, this expectation is reinforced by the observation that olivines in lunar basalts are depleted in these elements by a factor of over ten to a hundred when compared to their terrestrial counterparts, which cannot be reconciled by secondary processes at the lunar surface. Apollo 17 (high-Ti) olivines are especially depleted, with Ni contents of around 30 µg g^{-1} (Karner et al., 2003). By contrast, olivines found in mid-ocean ridge basalts typically have ca. 2000–3000 µg g^{-1} Ni even though their sources are sulfide-saturated (cf. Li et al., 2003). The Ni depletion in lunar olivines would be consistent with the retention of this element in a residual metal phase present in the lunar mantle. Interestingly, lunar olivine is V-rich compared to terrestrial olivines (Karner et al., 2006). Under more reducing conditions around the canonical mantle fO_2 of IW −1, V is predominantly trivalent, and becomes compatible into olivine (cf. Mallmann and O'Neill, 2009), which is entirely consistent with a reduced lunar mantle. Sutton et al. (1993) also identified the predominance of Cr^{2+} using X-ray absorption near edge spectroscopy (XANES) in lunar olivines from a low-Ti basalt sample (15555), which led them to conclude the olivine crystallized from a parental magma that had almost exclusively divalent Cr (i.e. easier to achieve at lower fO_2). Importantly, mineral/melt partitioning behavior is not expected to be affected by local processes like solar wind implantation of H, or by degassing of C. Moreover, neither process should affect the XANES valence determinations of V in olivine-hosted glass inclusions like those reported by Karner et al. (2006), given that these trace elements are hosted in glass surrounded, and thus protected by their olivine hosts. Based on these XANES data, Karner et al. (2006) suggested that most lunar basalts formed at fO_2 conditions between IW −1 and IW −2. A recent study by Zhang et al. (2024), who carried out V in spinel and olivine oxybarometry on samples from the Chang'e-5 lunar mission, concluded that the lunar mantle has likely experienced long-term reduction with an average fO_2 of IW −0.84 ± 0.65, well within uncertainty of the canonical value of IW −1 (Wadhwa, 2008).

Another line of evidence for a reduced lunar mantle is related to the oxidation state of Ti in lunar samples and their minerals. Titanium is exclusively tetravalent in terrestrial samples, but some trivalent Ti is present in lunar samples, as evidenced by recent XANES Ti K-edge studies of lunar samples. For example, Simon and Sutton (2018) have shown that lunar pyroxenes, ilmenites and armalcolites can have between 10 to 30 % of Ti^{3+}. These results are echoed by the experimental study by Leitzke et al. (2018) who determined the valence of Ti in olivine, pyroxene, armalcolite and ilmenite in their experiments and found that the proportion of 10–30 % of Ti^{3+} described by Simon and Sutton (2018) is reached between IW −1 and IW −1.8. Ballhaus et al. (2022), who carried out magmatic differentiation experiments under both oxidizing and reducing conditions, found that in Fe-metal saturated systems, SiO_2 enrichment only takes place after much higher degrees of fractional crystallization compared to more oxidized terrestrial magmas. These authors argued that their results are consistent with expectation from lunar basalts, which only very rarely show evidence of SiO_2 enrichment, and show the overall low viscosities that one would expect from high-FeO, low-SiO_2 magmas.

From what was discussed above, there is consistent and widespread evidence suggesting lunar basalts resulted from partial melting of mantle sources at fO_2 between IW −1 and IW −2. We thus find that it is reasonable to assume that the redox state of the lunar mantle is reflected by the oxygen fugacities recorded in lunar basalts and glasses, which is likely to be ∼IW −1 (cf. review by Wadhwa, 2008) to as reduced as IW −2 for the sources of some high-Ti basalts (Karner et al., 2006; Fonseca et al., 2014; Leitzke et al., 2016). Below, we will discuss the implications of such reduced sources, namely the thermodynamic viability of metal saturation in the lunar mantle.

3 Theoretical background and methods

3.1 Estimating metal compositions based on lunar oxygen fugacity

Assuming estimates of lunar fO_2 are correct (i.e. IW −1 or lower), it is possible to do a simple test of whether the lunar mantle can be metal-saturated by estimating the activity of Fe metal (a_{Fe}^{metal}) in lunar mantle sources using the following redox equilibrium reaction:

$$Fe_{metal} + 0.5\,O_2 = FeO_{SM} \quad (3)$$

where the subscript *SM* refers to silicate melt.

The equilibrium expression that describes Reaction (3) is given by:

$$\log K_{eq} = \log a_{FeO}^{SM} - \frac{1}{2}\log fO_2 - \log a_{Fe}^{metal} \quad (4)$$

where K_{eq} is the equilibrium constant for Reaction (3), and a_{FeO}^{SM} is the activity of FeO in mare basalts. Equation (4) can be rearranged to solve for $\log a_{Fe}^{metal}$ according to:

$$\log a_{Fe}^{metal} = \log a_{FeO}^{SM} - \frac{1}{2}\log fO_2 - \log K_{eq} \quad (5)$$

All the terms in the right-hand side of Equation (5) are either known (i.e. K_{eq} and fO_2), or can be calculated (i.e. a_{FeO}^{SM}). The a_{FeO}^{SM} can be derived from the known molar fraction of FeO in lunar mare melts, and the activity coefficient of FeO in silicate melts (γ_{FeO}^{SM}). The latter parameter has been shown to depend on silicate melt composition but is typically close to unity for depolymerized basaltic melts, and negatively correlates with melt TiO_2 content (O'Neill and Eggins, 2002). For high-Ti mare basalts γ_{FeO}^{SM} is thus slightly smaller than unity (ca. 0.85; O'Neill and Eggins, 2002). Holzheid et al. (1997) have suggested a higher value of γ_{FeO}^{SM} for basaltic melts of 1.7. However, O'Neill and Eggins (2002) investigated a wider range of silicate melt compositions when compared to Holzheid et al. (1997). Moreover, according to Equation (5), at any given fO_2 using higher values of γ_{FeO}^{SM} will result in systematically higher calculated a_{Fe}^{metal} when compared to using an γ_{FeO}^{SM} of around unity. In other words, the higher γ_{FeO}^{SM} is, the easier it is to reach high enough values of a_{Fe}^{metal} to ensure metal saturation. More recently, Wood and Wade (2013) parameterized γ_{FeO}^{SM} as a function of silicate melt composition, which did not include melt TiO_2, which is more relevant for lunar compositions. As such, we have opted to use the more conservative γ_{FeO}^{SM} of O'Neill and Eggins (2002) to calculate a_{Fe}^{metal}, as we consider their value estimates for TiO_2-rich compositions more representative of the behavior of FeO in lunar mare basalts.

In order to model the range of a_{Fe}^{metal} at lunar fO_2 for the sources of low- and high-Ti basalts we have used the average FeO contents of primitive Apollo 15 and 17 basalts (lunar data compendium), respectively, to calculate a_{FeO}^{SM}. We have assumed that Ni will have no effect on a_{Fe}^{metal} aside from one of dilution, given that mixing of Fe and Ni in the Fe-Ni binary follows Raoult's law for X_{Ni}^{metal} smaller than 0.3 (Maruyama and Ban-Ya, 1978). Furthermore, we have calculated a_{Fe}^{metal} for liquid Fe metal diluted with increasing amounts of S using the activity composition relationships of the Fe-FeS system as described by Buono and Walker (2011). With this information, it becomes feasible to ascertain the threshold at which fO_2 would need to decrease to achieve saturation of Fe-Ni metal with variable S contents. A summary of the parameters used in these calculations, for high- and low-Ti basalt sources, is given in Table 1.

The results of the a_{Fe}^{metal} vs. $\log fO_2$ models are shown in Figure 2 and allow for some key conclusions to be reached. Firstly, saturation in a pure Fe metal phase (i.e. $a_{Fe}^{metal} = 1$) is only possible on the more reduced end of the lunar fO_2 range described in the literature (IW −1.5 to IW −2 for low- and high-Ti basalt sources, respectively). The addition of Ni will alleviate these requirements and will allow metal saturation to take place at higher fO_2, albeit this is largely dependent on how much Ni is in the metal. Secondly, the addition of S to the residual metal will also result in lower values of a_{Fe}^{metal} (Buono and Walker, 2011), which predictably allows for metal saturation to be reached at higher values of fO_2. For example, if during partial melting the a_{Fe}^{metal} is around 0.7, which would be the case if residual metal contains ca. 12.5 wt% S, low- and high-Ti basalt sources are expected to be metal-saturated at IW −1.2 and IW −1.5, respectively. This fO_2 requirement for metal saturation in lunar mantle sources is far less stringent than that for pure Fe-metal and is closer to the canonical fO_2 value of IW −1 for the lunar mantle (Jones, 2004; Wadhwa, 2008).

Table 1. Parameters used for the calculation of the a_{Fe}^{metal} of high- and low-Ti mare basalts at an fO_2 of IW −1. Also calculated are the fO_2 of both types of lunar basalts in equilibrium with pure Fe metal, and an Fe-rich alloy that contains 10 wt% S. The FeO content of Apollo 15 (low-Ti) and Apollo 17 (high-Ti) mare basalts are averages taken from the lunar data compendium. γ_{FeO}^{SM} are taken from O'Neill and Eggins (2002), and activities of Fe in the Fe-S binary system were calculated using the activity composition relationships as described by Buono and Walker (2011).

	Low-Ti Apollo 15	High-Ti Apollo 17
FeO (wt%)	22	13.8
X_{FeO}	0.19	0.12
γ_{FeO}	1	0.85
log fO_2 (ΔIW) - a_{Fe} = 1	-1.5	-2
log fO_2 (ΔIW) - a_{Fe} = 0.7 (10 wt% S)	-1	-1.6
aFe (IW −1)	0.6	0.3

The question then becomes just how much Ni and S is the residual metal expected to have? Brenan et al. (2019) estimated that any Fe-S phase present in the lunar mantle should have up to ~12 wt% Ni, which would drop a_{Fe}^{metal} to ca. 0.9. This view is consistent with the observed Ni depletion in olivines from mare basalts (Karner et al., 2003), which are best explained if Ni is retained at their mantle source by a metal phase. Likewise, estimates for the S content of the silicate Moon range between 70–160 μg g^{-1} (cf. Chen et al., 2015; Hauri et al., 2015), so any presumptive residual metal phase would be expected to contain several wt% S. Moreover, the metallic melts in experiments by Brenan et al. (2019) are S-poor at IW −1 and below, with ca. 10 wt% S on average – i.e. very similar to the predictions of our preferred model metal composition. Such a composition would have its liquidus at 1600 to 1620 K (between 1 to 2 GPa; Buono and Walker, 2011). Given that the liquidi of primitive lunar melt compositions, like the orange, green and black glasses, range between ca. 1650 K (at 1 bar) and 1900 K (at 2.5 GPa for the refractory

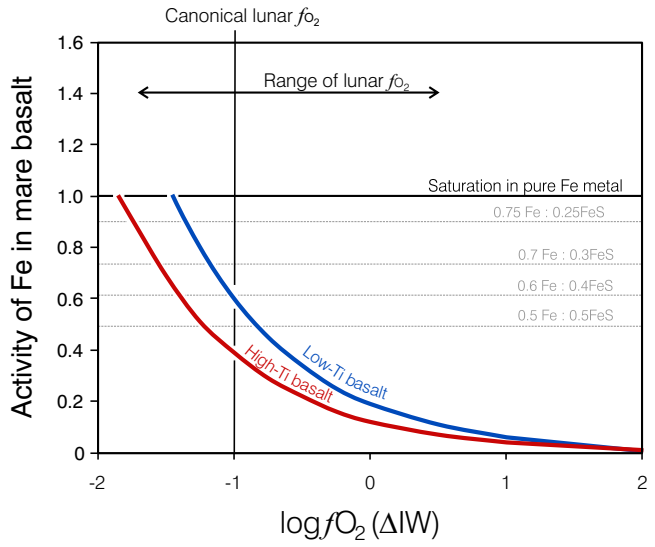

Figure 2. Activity of Fe (a_{Fe}^{metal}) in mare basalts as a function of fO_2 (given relative to the Fe-FeO reference redox reaction). Saturation in pure Fe metal (i.e. when $a_{Fe}^{metal} = 1$) is achieved at IW −1.45 and ca. IW −2, for low- and high-Ti basalts, respectively. However, saturation in a Fe-rich alloy with about 10 wt% S (i.e. 30 at% FeS) is expected to occur at IW −1.2 for low-Ti and at IW −1.5 for high-Ti basalts. Activities of Fe in metal calculated using thermochemical data from Buono and Walker (2011) and Barin (1995).

green glass; see Rai et al., 2019, and references therein), it is likely that the presumptive Fe-(Ni)-S residual metal was fully molten during mare basalt petrogenesis. To be clear, we consider any Fe-(Ni)-S liquid composition falling on the Fe-rich liquidus to the left of the Fe-FeS eutectic to consist of a S-poor metallic melt and not a sulfide liquid. Conversely, any composition falling on the right-hand side of that eutectic (i.e. S-rich) is considered a sulfide liquid. The eutectic of the Fe-FeS system sits at an X_{FeS}^{metal} of 0.7 at 3 GPa and 1200 K, and close to 0.9 at 1 bar and 1275 K (Buono and Walker, 2011), so under conditions relevant to the lunar mantle, any Fe-(Ni)-S residual metal likely falls on the metal-rich side of the eutectic.

As pointed out recently by Brenan et al. (2019), if during partial melting a mantle source is saturated in a S-poor Fe-(Ni)-S liquid, then SCSS in the melt will be lower than what it would otherwise be had it been saturated in a S-rich sulfide melt (Ding et al., 2018; Steenstra et al., 2018), reinforcing the expectation that lunar mantle sources could be metal saturated. Based on our calculations, the expected fO_2 of the lunar mantle (i.e IW −1 or lower), and the experimental constraints from Brenan et al. (2019), we predict that the residual metal present in lunar mantle sources should have up to 80 wt% Fe, 10 wt% Ni and ca. 10 wt% S. Based on estimates for the S content of the silicate Moon (ca. 80 µg g^{-1} S; Hauri et al., 2015), this would correspond to a modal fraction of metal in the lunar mantle between 0.05 and 0.1 wt%, depending on the exact Ni and S contents of the metal phase.

3.2 Experimental methods

Bulk compositions were prepared by initially mixing Mo, W, Pt, Pd, Rh, Ru, Os, Ir, and Re from Alfa Aesar acid solutions (20 % HCl, 1000 µg mL^{-1} concentration) with elemental sulfur powder (Alfa Aesar, 99.9 % purity) at a ratio of about 40–50 µg g^{-1}, except for experiment L150, which had ca. 500 µg g^{-1} each of Mo and W. After drying overnight at 60 °C, metallic powders of Fe and Ni (Alfa Aesar, 99.9 % purity) were added following proportions detailed in Table 2, using a procedure similar to that of Fonseca et al. (2024). Copper was not deliberately added to any composition, but was nevertheless identified in the experimental run products, presumably as impurities in the metallic powders used. The mixes were ground in an agate mortar and placed in 6 mm outer and 4 mm inner diameter SiO_2 glass tubes and sealed at 1 Pa under vacuum using a hydrogen-oxygen torch. Subsequently, the samples were heated to 900 °C and held overnight to form crystalline sulfide phases. After crushing and repeating the process for homogeneity, the pre-reacted sulfides were mixed with a synthetic basalt glass powder (MPxAB and MTEP5) or a synthetic lherzolite powder (MP1KLB-1) in ratios of 60 wt% metal and 40 wt% silicates and 40 wt% metal and 60 wt% silicates, respectively. Unfortunately, these procedures had the negative side effect that Re and Os were partially lost during the drying steps, which resulted in lower than expected concentrations of these elements in the experimental run products. The composition of the basalt powder was synthesized after a high-Mg Low-Ti mare basalt (12005; Meyer, 2010), and the lherzolite is similar to the KLB-1 spinel lherzolite (Takahashi, 1986). The silicate starting materials were prepared from analytical grade oxides, carbonates, and hydroxides using an established routine as described in detail by Beyer et al. (2021). The Apollo basalt glass was not reduced, whereas the KLB-1 slag was reduced at 1000 °C in a CO_2-CO gas flow overnight to an oxygen fugacity one log unit above the iron-wüstite reference redox equilibrium.

High-pressure experiments were conducted utilizing an end-load piston cylinder apparatus (Voggenreiter Mavopress LPC 250/30) and a 630 t Walker-style multi-anvil apparatus at Ruhr-University Bochum. Both machines were calibrated using well-characterized phase transitions, namely: quartz-coesite (1200 °C), jadeite-albite-quartz (1000 °C), fayalite-quartz-ferrosolite (1000 °C) and DTA of gold for the piston-cylinder; and coesite-stishovite (1200 °C), $CaGeO_3$ garnet-perosvkite (1200 °C), and the melting point of gold for the multi-anvil apparatus. The pressure for the piston cylinder is reproducible within 0.08 GPa, whereas for the multi-anvil the pressure is reproduced with an uncertainty of 0.3 GPa. With the exception of experiment L150, which used a capsule fashioned from crushable MgO, all experiments featured capsules machined from single crystal MgO (high purity MgO, sourced from Plano GmbH). Experiment L180, featured a three chamber single crystal MgO capsule, where only the C content of the metal was varied (0, 2, 5 wt% C in metal for experiments L180A, B and C, respectively). In the piston cylinder experiments, specimens were loaded into 1/2" talc-Pyrex pressure cells featuring a straight

Table 2. Starting compositions for the different experiments. A lunar basaltic glass was synthetized to reproduce a primitive, high MgO Apollo 12 low-Ti mare basalt 12005 (Meyer, 2010). Kilborne hole peridotite (KLB-1) synthesized after Takahashi (1986). All values are given in wt%, unless stated otherwise.

Metals	MP1AB	MP2AB	MP3AB	MP4AB	MTEP5	MP1KLB-1
Fe	85	80	75	84	84	85
S	10	15	20	10	10	10
Ni	5	5	5	5	5	5
C				1	1	
metal/sil	60:40	60:40	60:40	60:40	70:30	40:60

	Lunar basalt	KLB-1
SiO_2	42.01	44.15
TiO_2	2.9	0.19
Al_2O_3	5.36	3.72
Cr_2O_3	0.76	0.3
FeO	22.51	8.47
MgO	20.19	39.36
CaO	6.38	3.6
Na_2O		0.32
K_2O		0.03

graphite heater and crushable MgO plugs and liners. To minimize friction between the pressure cell and the tungsten-carbide bore, the assembly was enveloped in PTFE foil. Temperature monitoring during runs was achieved using either a type-D thermocouple ($W_{97}Re_3$-$W_{75}Re_{25}$) or Type-C thermocouple ($W_{95}Re_5$-$W_{75}Re_{25}$), positioned axially within 1 mm of the sample capsule. Pressure and temperature were simultaneously raised to the desired final conditions and maintained between 30 to 47 min (Table 3). All experiments were terminated by cutting the power to the heater.

For the single experiment on the multi-anvil press, a 14/8 (14 mm octahedron edge length, 8 mm truncated edge length) octahedral pressure medium was used. This octahedron consisted of Cr_2O_3-doped magnesium oxide (from Ceramic Substrates, Isle of Wight), a zirconium oxide insulator (OZ8C, Mino Ltd., Japan), and a stepped graphite heater. Crushable MgO (RM98TE, Rauschert GmbH) were used inside the pressure medium. To monitor temperature, we inserted a Type-C thermocouple axially using a quadbore alumina tube, surrounded by a crushable MgO sleeve. Cavities around the thermocouple tip were filled with alumina powder to protect it during compression and prevent deformation of the pressure assembly. The experiment was compressed to 4.5 GPa pressure within three hours. The temperature was ramped up to its target value at a rate of ca. 100 °C min^{-1} and maintained at the desired temperature for 10 min. Quenching was achieved by cutting off electrical power, causing the temperature to drop to below 80 °C within 2–3 s (monitored by the Eurotherm temperature controller). For our standard 14/8 stepped graphite assembly, we calculated the thermal gradient based on the thermal properties and post-run geometry of the experiment using the code provided by Hernlund et al. (2006). Accordingly, we expect a temperature gradient between the TC junction and center of the capsule of ~20 °C at 1900 °C. All experimental conditions are listed in Table 3.

After the experiments, samples were embedded in epoxy and longitudinally ground to reveal a cross-section. High-quality polished surfaces were obtained through a series of epoxy-bound diamond sanding plates and hard polishing discs with diamond paste down to 1 µm with a water-free lubricant/cooling liquid (Struers DP Blue). All samples were stored in a desiccator to prevent oxidation of the exposed metal.

3.3 Analytical methods

The textures of sulfide phases in each experiment were examined using optical and electron microscopy. Specifically, a JEOL JSM-7200F SEM at the Center for Interface-Dominated High-Performance Materials (ZGH) of Ruhr-University Bochum (Germany) was used. The major element composition of metal and silicate phases in each experiment was determined using a Cameca Field-Emission SXFiveFE EMPA, at the Institute for Geology, Mineralogy, and Geophysics of Ruhr-University Bochum (IGMG). Measurements were conducted at 15 kV accelerating voltage and 15 nA beam current, using a 1–20 µm-diameter beam to account for quenched metallic melt heterogeneity. Samples and reference materials were coated with a 10 nm carbon coat to ensure reliable measurements of their oxygen content. Reference materials included pyrite, chalcopyrite, and pentlandite for S, Fe, and Ni, respectively, utilizing peak-to-background calibrations. Oxygen was measured using a PC0 light-element detector crystal, and its content in the metal referenced to periclase (MgO), while oxygen backgrounds were monitored on nominally oxygen-free phases (metals and sulfide reference materials). The detection limit for oxygen under these analytical conditions was 0.1 wt%. Major

Table 3. Summary of experimental run conditions. *Oxygen fugacities were calculated using the activity composition relations of the Fe-FeS system by Buono and Walker (2011). Uncertainties for the calculated fO_2 were propagated through a Monte Carlo simulation with 10,000 samples using measured uncertainties associated with the electron microprobe data, and those associated with the calculation of the activity coefficients in the Fe-FeS system from Buono and Walker (2011).

Run	P GPa	T °C	duration min	log fO_2* ΔIW	±	starting material	capsule	comment
I83	1.5	1500	30	-1.14	0.02	MP2AB	MgO SC	
L150	1.5	1500	47	-1.29	0.02	MTEP5	MgO crushable	only W,Mo, C-bearing (1 wt%)
L160	1.5	1500	30	-1.27	0.01	MP1AB	MgO SC	
L161	1.5	1500	30	-1.11	0.03	MP4AB	MgO SC	C-bearing (1 wt%)
L162	1.5	1500	30	-0.32	0.07	MP3AB	MgO SC	
L181A	1.5	1500	30	-1.24	0.04	MP2AB	MgO SC	
L181B	1.5	1500	30	-0.58	0.06	MP2AB	MgO SC	+ 2 wt% C
L181C	1.5	1500	30	-0.74	0.06	MP2AB	MgO SC	+ 5 wt% C
E398	4.5	1900	10	-1.98	0.04	MP1KLB-1	MgO SC	only W,Mo

element contents for each of the experimental run products can be found in Table 4.

Experimental run products were measured for their HSE, Mo and W abundances using an ESL NWRImageGEO 193 nm excimer laser ablation system coupled to an Agilent 8900 triple quadrupole ICP-MS run in single-quadrupole mode (LA-ICP-MS). Following Wohlgemuth-Ueberwasser et al. (2007), laser fluence and repetition rate were kept low (4–5 J cm^{-2}, and 5 Hz, respectively) in order to enhance the ablation yield in the metallic melts, and set to 7 J cm^{-2}, and 10 Hz for the measurement of the silicates. Spot sizes varied between 40 and 70 µm depending on the size of the phases measured, namely the size of the metal blebs present in each experiment. Sample aerosols were carried to the mass spectrometer using a constant He flow of 1000 mL min^{-1}. Depending on the analyte (Mo & W, HSE) in the experimental run products, different reference materials were used for external calibration. We used the synthetic Ni-bearing pyrrhotite, PGE-Ni7b (described in Wohlgemuth-Ueberwasser et al., 2007), for the quantification of the HSE, whereas NIST-SRM-612 (Jochum et al., 2011) was used for Mo and W. The internal standard used for normalization was always ^{57}Fe. The count rates for the nuclides of ^{29}Si, ^{34}S, ^{43}Ca, ^{57}Fe, ^{61}Ni, ^{63}Cu, ^{65}Cu, ^{95}Mo, ^{99}Ru, ^{101}Ru, ^{103}Rh, ^{105}Pd , ^{106}Pd, ^{182}W, ^{185}Re, ^{189}Os, ^{193}Ir and ^{195}Pt were measured. Each nuclide was measured employing 33 ms of dwell time (ca. 630 ms for the whole mass range) and each laser spot was measured for 20 seconds on the gas background, and 30 seconds with active ablation on the sample. Measurements were carried out via standard/sample bracketing, with no more than 15 spots measured between each standard measurement. Data reduction was carried out using the procedure described by Longerich et al. (1996) in similar fashion to what is described by Fonseca et al. (2017). Possible argide molecular interferences on ^{101}Ru (^{61}Ni^{40}Ar$^+$), ^{103}Rh (^{63}Cu^{40}Ar$^+$) and ^{105}Pd (^{65}Cu^{40}Ar$^+$) were evaluated and found to be negligible given the good agreement between concentrations obtained from multiple isotopes of the same element (i.e. ^{99}Ru and ^{108}Pd). The trace element contents for metal and silicate melt for each experiment are given in Table 5. Examples of typical LA-ICP-MS transient signals are shown in the Supplementary Material in Figure S1.

The limits of detection (LOD) were determined following the methodology outlined by Longerich et al. (1996), and consisted of the 3σ of a nominally HSE, Mo, and W-free signal divided by the measurement sensitivity of each element. Over multiple measurements, the calculated LOD (in ng g^{-1}) were 4 for Mo, 1 for W, 1–2 for Pd, 1.7–1.8 for Pt, 0.7–0.8 for Rh, and 1.3–1.4 for Re. These calculated LODs are only slightly lower than those determined recently by Zhang and Li (2021) for Pt and Pd (3 to 7 and 3 to 8 ng g^{-1}, respectively) using a single quadrupole ICP-MS (an Agilent 7900), and comparable laser ablation system (Analyte HE 193 nm ArF Excimer Laser). The calculated LOD for Ru, Os, and Ir were difficult to assess due to their gas backgrounds being zero in most measurements. Nevertheless, the maximum determined LOD for Ru, Os, and Ir were 0.9, 1.9, and 0.7 ng g^{-1}, respectively, even if the minimum calculated values were essentially a more unrealistic zero. As the measured concentrations for these elements were on occasion close to their maximum calculated LOD, caution should be taken when adopting these values and as well as any calculated partition coefficients from these data. Determining Cu concentrations in silicate melt proved problematic, as values obtained from ^{65}Cu were approximately 40 % higher than those from ^{63}Cu. In hindsight, this discrepancy likely arises from an isobaric molecular interference of ^{40}Ar^{25}Mg$^+$ on ^{65}Cu, leading to artificially elevated count rates for that nuclide. Unfortunately, ^{63}Cu is also subject to its own isobaric interferences, including the relatively minor ^{27}Al^{36}Ar$^+$ and the more significant ^{47}Ti^{16}O$^+$, given that our starting compositions contained several wt% TiO_2 (see Table 4). Consequently, we do not consider any $D_{Cu}^{metal/sil}$ values from our experiments to be reliable.

Table 4. Summary of major element contents of each of the experimental run products. All values given in wt%. Uncertainties consist of standard errors of the mean. *Totals include trace elements. **A smaller metal bleb at the "colder" bottom of that capsule had higher S content (12.7 wt%) but was interpreted to be quench modified and not representing equilibrium conditions. ***C was not measured.

Metal

Run	n	Fe	±	Ni	±	S	±	O	±	Total*
I83	19	85.0	0.3	7.8	0.1	7.1	0.4	0.19	0.01	100.1
L150	12	88.1	0.4	5.7	0.1	4.6	0.5	0.17	0.01	98.6
L160**	12	87.3	0.3	8.4	0.1	3.5	0.2	0.09	0.05	99.3
L161	13	84.0	0.7	6.3	0.1	8.4	0.7	0.30	0.10	99.0
L162	20	72.3	0.9	5.8	0.3	21.8	1.1	0.60	0.10	100.5
L181A***	20	84.6	0.4	8.3	0.2	6.6	0.5	0.17	0.01	99.7
L181B***	18	85.6	0.4	7.6	0.3	1.3	0.1	0.06	0.01	94.6
L181C***	25	85.1	0.5	7.3	0.1	1.8	0.6	0.08	0.01	94.3
E398	29	80.3	0.2	5.4	0.1	12.4	0.2	0.53	0.04	98.6

Silicate glass

Run	n	SiO_2	±	TiO_2	±	Al_2O_3	±	Cr_2O_3	±	FeO	±	MgO	±	CaO	±	Total*
I83	23	40.5	0.2	3.3	0.2	7.2	0.4	0.53	0.01	24.7	0.2	15.6	1.2	8.6	0.5	100.4
L150	15	40.2	0.1	3.3	0.1	7.1	0.2	0.50	0.007	22.8	0.1	16.3	0.7	9.2	0.3	99.4
L160	20	38.5	0.1	3.0	0.1	12.4	0.3	0.43	0.01	23.2	0.2	15.1	0.2	7.8	0.2	100.4
L161	38	35.1	0.2	3.9	0.3	8.0	0.5	0.53	0.02	25.2	0.3	18.6	1.4	9.8	0.7	101.1
L162	40	40.7	0.2	3.4	0.2	7.4	0.3	0.59	0.01	25.7	0.3	13.7	1.0	8.5	0.4	100.0
L181A***	15	40.3	0.4	4.3	0.4	8.9	0.7	0.58	0.05	20.6	0.3	12.4	2.3	11.4	1.0	98.5
L181B***	19	40.8	0.3	3.4	0.2	7.4	0.4	0.50	0.01	22.3	0.2	16.4	1.5	8.7	0.6	99.5
L181C***	17	40.3	0.2	4.7	0.2	10.2	0.5	0.51	0.01	17.8	0.2	12.3	1.5	12.4	0.7	98.2
E398	17	38.9	0.3	0.25	0.4	5.2	0.7	0.22	0.01	8.9	0.3	41.3	1.7	5.2	0.8	100.0

Olivine

Run	n	SiO_2	±	TiO_2	±	Al_2O_3	±	Cr_2O_3	±	FeO	±	MgO	±	CaO	±	Total*
I83	12	39.7	0.08	0.17	0.08	0.21	0.08	0.31	0.01	17.7	0.1	40.5	0.3	0.46	0.06	99.1
L160	15	39.4	0.07	0.17	0.05	0.25	0.07	0.32	0.01	18.4	0.1	40.4	0.3	0.42	0.04	99.4
L161	10	40.4	0.05	0.07	0.01	0.15	0.01	0.232	0.004	13.53	0.08	45.1	0.1	0.44	0.02	99.9
L162	13	39.99	0.03	0.07	0.01	0.16	0.10	0.255	0.004	17.3	0.1	41.1	0.2	0.33	0.01	99.2

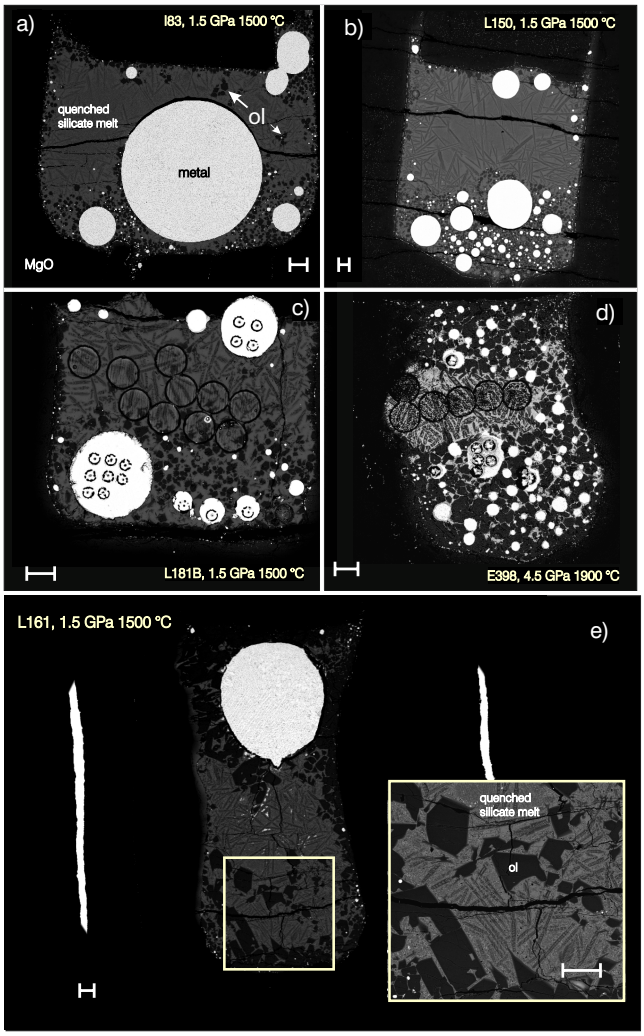

Figure 3. Backscatter electron image of typical experimental run products for piston cylinder experiments I83 (a), L150 (b), L181B (c), and L161 (e), and the single multi-anvil experiment E398 (d). In all experiments, metal is shown mostly concentrated into larger spherical blebs with several 100 µm diameter, whereas silicate melt quenched to a spinifex-like dendritic texture. Metallic blebs shows evidence of immiscibility during quenching, with subsidiary parallel lamellae with higher S content. Some experiments also featured liquidus olivine (c, d and e), as opposed to the quenched olivine crystals seen associated with the spinifex-like texture. Scale bars in each panel represent 100 µm.

4 Results

4.1 Experimental run products

In a typical experimental run, the products consist of quenched round blebs of metallic melt, as shown in Figure 3, alongside spinifex-like silicate glass. The quenched metallic melts exhibit fine S-rich exsolutions within a more Fe-Ni rich matrix (Fig. 3a). Additionally, all experiments feature regions where small, µm-sized metallic melt nuggets are associated along grain boundaries of dendritic quench olivine. To mitigate potential contamination by metallic nuggets and therefore biased results, these regions were avoided during the measurement of the silicate melt's siderophile element abundances. In some experiments, small crystals of liquidus olivine, depicted in Figure 3e (inset), were also present. The quenched silicate glass in these regions contained multiple trapped Fe-S blebs. Experiment L181A was situated in the colder part of a multi chamber piston cylinder assembly, and displayed a large amount of liquidus olivine and associated small-scale Fe-S metal blebs, which made analysis of that particular sample difficult. Further examples of typical textural features of experimental run products are shown in the Supplementary Material in Figure S2.

4.2 Metal/silicate partitioning results

Calculated metal/silicate partition coefficients from our experiments are shown in Figure 4 and summarised in Table 5. With no exception, $D_i^{metal/sil}$ decreases with increasing S content. Partitioning of Mo and W between Fe-S liquid and silicate melt shows a clear negative correlation with S content, with values ranging between ca. 560 to 206 for Mo, and between 8 and 0.32 for W (Fig. 4a).

All HSE behave similarly with increasing S content in metal, with $D_i^{metal/sil}$ ranging in the tens of thousands (except for Re) to a few thousands at high S contents in metal (Figure 4b,c; Table 5). In the case of Re, and to a lesser extent Os, because these elements were lost during the initial stages of sample preparation due to volatile loss, their concentrations were much lower in all experiments. This resulted in fewer Re partitioning data being obtained, as Re was often below detection limit during the majority of LA-ICP-MS measurements of the quenched silicates. As such, only partitioning data for the more S-rich experiments L161 and L162 are given, with $D_{Re}^{metal/sil}$ of 5789 and 5000, respectively. Rhenium partitioning data were also obtained for the C-bearing experiments L181B and L181C (see below).

Values of $D_{Ni}^{metal/sil}$ and $D_S^{metal/sil}$ are shown in Figure 4d. Nickel partition coefficients are shown to decrease with increasing S content of the Fe-S liquid, in line with the HSE, Mo and W. The partitioning of Cu (not shown) does not show a clear correlation with S content of Fe-S liquid. The reason for this is unclear, but it may have to do with difficulties in accurately measuring the Cu content of the glass using LA-ICP-MS due to the presence of isobaric interferences (see methods, Section 3.3) leading to inaccurate $D_{Cu}^{metal/sil}$. Sulfur content of the silicate melt increases with the S content of the Fe-S liquid, with a corresponding increase in $D_S^{metal/sil}$. This result is unsurprising as S solubility in silicate melt is known to positively correlate with the a_{FeS}, as well as with the fO_2 of the system (c.f. Mavrogenes and O'Neill, 1999, and Figure S3 in the Supplementary Material), which is the case in our experiments.

Experiments (I83, L181B, and L181C) were doped with 1, 2.5, and 5 wt% of C, respectively (added as graphite

Table 5. Trace element content of experimental run products (in $\mu g\,g^{-1}$), and partition coefficients between liquid Fe-S metal and silicate melt. Data in brackets are considered outliers, or experiments where LA-ICP-MS signal contamination was unavoidable. *Major element in metal (see Table 4).

Sample	Ni*	±	Cu	±	Mo	±	W	±	Pt	±	Pd	±
Metal												
I83	*	*	73	4	26	1	9.7	0.6	14	1	47	1
L150	*	*	(353)	(63)	517	5	501	7	-	-	-	-
L160	*	*	122	7	67	1	37	1	64	4	76	4
L161	*	*	84	5	84	1	33.6	0.4	66	4	62	4
L162	*	*	105	8	130	3	21	2	49	4	63	3
L181A	*	*	58	3	21	2	6.9	0.7	20	2	56	2
L181B	*	*	32	2	6.4	0.5	3.8	0.3	31	3	54	4
L181C	*	*	(89)	(22)	7	1	6	1	13	3	46	7
E398	*	*	22	1	223	6	411	105	-	-	-	-
Silicate melt												
I83	43	2	0.77	0.02	0.062	0.004	8.6	0.1	0.005	0.002	0.008	0.001
L150	97	8	1.9	0.3	1.1	0.1	64	1	-	-	-	-
L160	33	3	1.8	0.2	0.12	0.02	8	1	0.005	0.001	0.0032	0.0002
L161	44	5	1.8	0.1	0.26	0.02	22	1	0.006	0.001	0.004	0.001
L162	84	4	1.1	0.1	0.63	0.01	66	0.2	0.008	0.002	0.008	0.002
L181A	120	48	1.2	0.1	(0.14)	(0.05)	(6.2)	(0.1)	(0.3)	(0.2)	(0.1)	(0.08)
L181B	84	8	1.52	0.03	0.044	0.005	5.09	0.06	0.07	0.03	0.022	0.007
L181C	791	134	2	0.1	0.5	0.1	4.3	0.5	2.9	0.9	0.3	0.1
E398	66	5	0.6	0.02	0.66	0.04	34	2	-	-	-	-
Metal/silicate partition coefficients												
I83	1814	88	95	6	419	31	1.1	0.1	2800	1138	5875	745
L150	588	50	186	44	470	43	7.8	0.2	-	-	-	-
L160	2545	233	68	8	558	93	4.6	0.6	12800	2682	23750	1941
L161	1432	164	47	4	323	25	1.5	0.1	11000	1951	15500	4002
L162	690	49	95	11	206	6	0.32	0.03	6125	1611	7875	2004
L181A	692	277	48	5	(150)	(55)	(1.1)	(0.1)	(66.7)	(44.9)	(560)	(448)
L181B	905	93	21	1	145	20	0.75	0.06	443	195	2455	802
L181C	(92)	(16)	(45)	(11)	(14)	(3.4)	(1.4)	(0.3)	4	2	153	56
E398	818	64	37	2	338	22	12	3	-	-	-	-

(continued overleaf)

powder), to test the effect that small amounts of carbon in metal have on the partitioning behavior of Mo, W, and the HSE. Any residual metal present in the lunar mantle is likely the source of the C found in lunar mare basalts, so it is worthwhile to test its effect on $D_i^{metal/sil}$. The addition of C results in clearly lower $D_{Mo,W}^{metal/sil}$ for similar S contents in the metallic melt, but also lower $D_{HSE}^{metal/sil}$ (see Figure S1 in the Supplementary Material). However, the exceptionally low $D_{HSE}^{metal/sil}$ values observed in the C-bearing experiments (often below 1000) raise concerns. It remains unclear whether these values truly reflect equilibrium partitioning or are instead influenced by the formation of nano-nuggets in the silicate melt, which are difficult to detect and quantify (see Supplementary Figures S1 and S2). Therefore, while we report these data for completeness, we do not consider them further in our analysis due to the uncertainty surrounding their reliability.

One single experiment was carried out at 4.5 GPa and 1900 °C (E398) in order to approximate lunar core formation conditions. This experiment was only doped with Mo and W, and not with any HSE, and yielded the highest $D_W^{metal/sil}$ (12 ± 3), and intermediate $D_{Mo}^{metal/sil}$ (338 ± 22) compared to other experiments, except for the C-bearing experiments where, as mentioned all $D_i^{metal/sil}$ were lower compared to C-free experiments.

5 Discussion

5.1 Comparison to previous experimental studies

Due to their low solubility in silicate melts, HSE partitioning studies often rely on starting materials doped with concentrations far exceeding those found in natural samples. This raises concerns about whether partitioning data adhere to Henry's law, particularly regarding the independence of HSE partition coefficients from overall concentration. While studies on HSE partitioning between liquid and solid metals generally follow Henry's law (Chabot et al., 2003), Zhang and Li (2021) demonstrated that HSE partitioning between sulfide and silicate melts deviates from this behavior at high HSE concentrations. Their study reported an approximately 100,000-fold increase in partition coefficients ($D_{Pt}^{sul/sil}$ and

Table 5. (continued)

Sample	Rh	±	Ru	±	Os	±	Ir	±	Re	±	S*	±
Metal												
I83	18.9	0.4	15	0.3	3.1	0.1	4	0.1	2.1	0.1	*	*
L150	-	-	-	-	-	-	-	-	-	-	*	*
L160	45	2	50	3	19	2	23	2	9	1	*	*
L161	38	2	43	2	22	1	23	2	11	1	*	*
L162	27	2	35	5	22	2	22	2	15	2	*	*
L181A	24	1	21	1	5.4	0.6	7.6	0.6	3.7	0.3	*	*
L181B	18	2	13	2	3.4	0.5	5.9	0.6	2.4	0.4	*	*
L181C	10	3	9	2	1.8	0.4	4.8	0.9	1.1	0.3	*	*
E398	-	-	-	-	-	-	-	-	-	-	*	*
Silicate melt												
I83	0.001	0.0005	0.001	(0.0005)	(0.001)	(0.0001)	-	-	0.003	(0.001)	1500	20
L150	-	-	-	-	-	-	-	-	-	-	1400	100
L160	0.0015	0.0004	0.0023	0.0003	0.0021	0.0002	0.0006	0.0001	bdl	bdl	2700	100
L161	bdl	bdl	0.002	0.001	0.0012	0.0001	0.0007	0.0001	0.002	0.001	2600	200
L162	0.003	0.001	0.007	0.003	0.0019	0.0004	0.0021	0.0007	0.003	0.001	2200	100
L181A	(0.002)	(0.001)	(0.003)	(0.001)	(0.002)	(0.001)	(0.004)	(0.003)	(0.006)	(0.002)	1450	40
L181B	0.009	0.005	0.01	0.005	0.004	0.002	0.008	0.005	0.003	0.001	1920	20
L181C	0.16	0.03	0.2	0.1	0.09	0.03	0.7	0.2	0.17	0.05	2200	100
E398	-	-	-	-	-	-	-	-	-	-	1470	40
Metal/silicate partition coefficients												
I83	18900	9458	15000	7506	(3100)	(326)	-	-	700	236	47	3
L150	-	-	-	-	-	-	-	-	-	-	33	4
L160	30000	8110	21739	3121	9048	1794	38333	7206	-	-	13	1
L161	-	-	21500	10796	18333	1740	32857	5495	5789	2583	32	4
L162	9000	3073	5000	2259	11579	2655	10476	3620	5000	1795	99	7
L181A	(11950)	(5988)	(7000)	(2357)	(2700)	(1383)	(1900)	(1433)	(617)	(212)	46	4
L181B	2000	1133	1300	680	850	443	738	467	800	298	7	1
L181C	63	22	45	25	20	8	7	2	6	3	8	3
E398	-	-	-	-	-	-	-	-	-	-	84	3

$D_{Pd}^{sul/sil}$) over a concentration range from tens of $\mu g\,g^{-1}$ to wt% levels, highlighting a strong dependence on doping levels. These findings echo similar observations raised by Crocket et al. (1997) and Fleet et al. (1999), who also observed a correlation between $D_{PGE}^{sul/sil}$ and the Platinum Group Element (PGE) concentrations in sulfide melt in their experiments. While these earlier studies only noted a "statistical significant correlation" between $D_{PGE}^{sul/sil}$ and PGE concentrations, Zhang and Li (2021) attributed this deviation to a decrease in $\gamma_{Pt,Pd}^{sul}$ with increasing Pt and Pd concentration.

Following their approach, we limited HSE additions to 20–50 $\mu g\,g^{-1}$ in our FeNi ± S starting mixtures to ensure compliance with Henry's law as closely as possible. This also allowed us to avoid recalculating our data to infinite dilution using activity-composition relationships that may not accurately reflect the petrological system studied, as well as minimizing large extrapolations from highly doped to dilute HSE concentrations.

As shown in Figure 5, partition coefficients for the HSE are generally at least an order of magnitude lower than previously published values (Brenan et al., 2019; Laurenz et al., 2016), except for the Pt and Pd dataset of Zhang and Li (2021). In fact the $D_{Pt,Pd}^{sul/sil}$ of Zhang and Li (2021) with similar Pt and Pd concentrations in their sulfide liquids to our Fe-S liquids, fall on the continuation of the trend defined by our own measured $D_{Pt,Pd}^{metal/sil}$ (Fig. 5). Laurenz et al. (2016) investigated the effect of sulfur on the metal-silicate partitioning of Pt, Pd, Ru, and Ir, finding – consistent with our study – that increasing sulfur content in Fe-S liquid reduces $D_{HSE}^{metal/sil}$ for all studied HSE. However, with the exception of Pd, all $D_{HSE}^{metal/sil}$ values reported by Laurenz et al. (2016) are considerably higher than those measured in our experiments (Figure 5a,b). The experiments of Laurenz et al. (2016) that assessed the effect of S on $D_{HSE}^{metal/sil}$ were conducted at higher temperatures and pressures (2200 °C, 11 GPa) than ours and involved doping with wt% levels of HSE. This makes it difficult to isolate the individual effects of these parameters on $D_{HSE}^{metal/sil}$. However, their study demonstrated that within their broader experimental conditions (2100–2400 °C, 7–21 GPa), HSE partitioning either decreases with temperature (for Pt, Ir, and Ru) or remains temperature-insensitive (Pd). Additionally, only $D_{Pt}^{metal/sil}$ increases with pressure, while the partitioning of other HSE appears unaffected by this parameter. Thus, the significantly higher $D_{HSE}^{metal/sil}$ values reported by Laurenz et al. (2016) likely result from the higher HSE concentrations

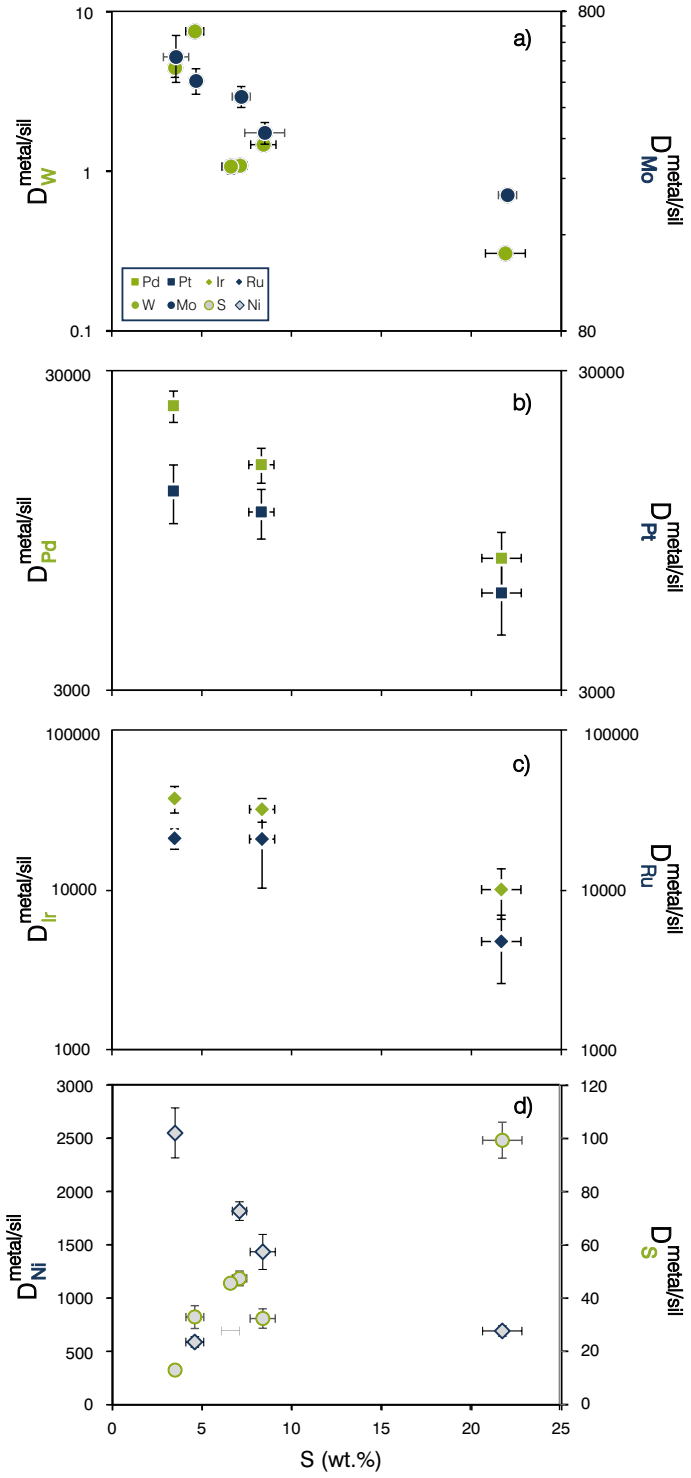

Figure 4. Partitioning of Mo, W, Pt, Pd, Ru and Ir between metallic melt and silicate melt as a function of the S content of the metallic melt. All experiments shown with closed symbols are C-free, whereas the sole C-bearing experiment (I83) is shown with open symbols. All experiments were carried out at 1500 °C and 1.5 GPa. Calculated oxygen fugacities are shown in Table 2

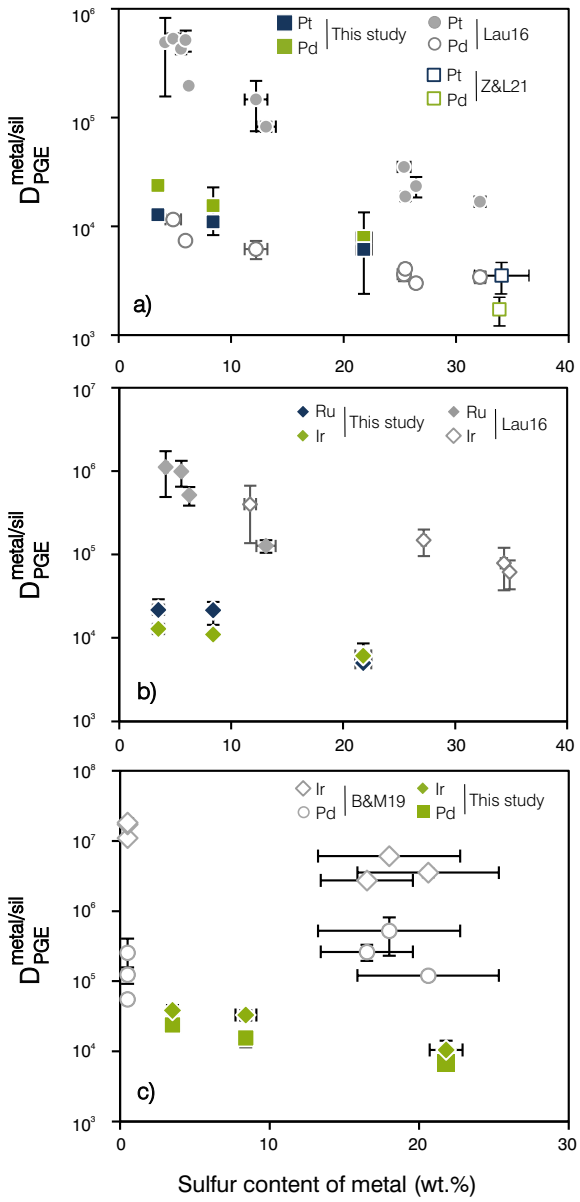

Figure 5. Comparison between our partitioning data for Pt, Pd, Ru and Ir and literature data for a) Pd and Ir from Laurenz et al. (2016); Zhang and Li (2021); for b) Ru and Ir from Laurenz et al. (2016) and c) Pd and Ir from Brenan et al. (2019) as a function of S content of the Fe-S liquid. See text for discussion.

in their metallic melts compared to our study, further supporting deviations from Henry's law.

This conclusion is reinforced by the data from Brenan et al. (2019), who conducted experiments using similar Fe-S liquid and silicate melt compositions at comparable pressures and temperatures (1 GPa and 1400 °C). The main distinction between our study and that of Brenan et al. (2019) is the amount of HSE dopant in the starting compositions – thousands to tens of thousands of μg g^{-1} in Brenan et al. (2019) compared to 20–50 μg g^{-1} in our study – which is consistent with their higher measured $D^{metal/sil}_{HSE}$ values (Fig. 5c). The one exception to this trend is $D^{metal/sil}_{Pd}$ from Laurenz et al. (2016), which closely matches our data (Fig. 5a) but is significantly lower than values reported by Brenan et al. (2019) at similar S contents. It is possible that at the higher pressures (7–21 GPa) of Laurenz et al. (2016),

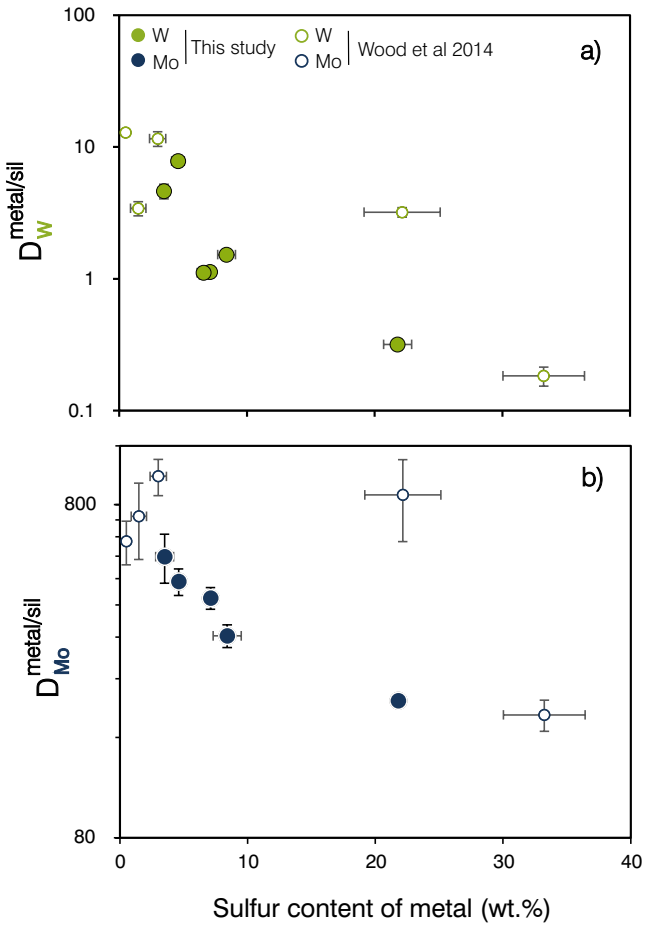

Figure 6. Comparison between our partitioning data for Mo (a) and W (b) and literature data from Wood et al. (2014).

$\gamma_{Pd}^{Fe\text{-}S\ metal}$ remains insensitive to Pd concentration in the Fe-S liquid, whereas at the lower pressures of our experiments and those of Brenan et al. (2019), this is not the case. Laurenz et al. (2016) sought to address the likely deviation from Henry's law in their experiments by correcting their data to infinite dilution, which only resulted in a modest average 0.2 log unit increase in their measured $D^{metal/sil}_{HSE}$. Assuming our data and that the conclusions by Zhang and Li (2021) are correct, then correcting the partitioning data to infinite dilution for the HSE may not result in a reliable outcome. Considering these observations, our results extend the findings of Zhang and Li (2021), demonstrating that HSE partitioning deviates from Henry's law at high dopant levels, including in the partitioning between liquid metal and silicate melt.

Interestingly, values of $D^{metal/sil}_{Mo,W}$ vary with the sulfur content of the liquid metal but appear unaffected by the amount of Mo and W doped. Experiment L150 (4.6 ± 0.5 wt% S), which contained ~500 µg g^{-1} of Mo and W, yielded $D^{metal/sil}_{Mo}$ and $D^{metal/sil}_{W}$ values similar to those of experiment L160 (3.5 ± 0.2 wt% S), which had comparable sulfur contents in the liquid metal ($D^{metal/sil}_{Mo}$ = 470 ± 43 vs. 558 ± 93, and $D^{metal/sil}_{W}$ = 7.8 ± 0.2 vs. 4.6 ± 0.6, respectively). These results suggest that, unlike the HSE, Mo and W partitioning between liquid metal and silicate melt follows Henry's law over the studied concentration range. This behavior is expected given the low activity coefficients and high solubilities of Mo and W in silicate melt (O'Neill and Eggins, 2002; O'Neill et al., 2008). With the exception of one outlier at 22 wt% S, our results align well with those of Wood et al. (2014), as trends between $D^{metal/sil}_{Mo}$, $D^{metal/sil}_{W}$, and sulfur content in Fe-S liquid broadly overlap (Fig. 6). This agreement holds despite the slightly higher temperatures (1650 °C) and much higher W and Mo concentrations (up to several wt%) in their experiments, further supporting that Mo and W partitioning follows Henry's law over a wider concentration range in metal compared to the HSE. We also considered W and Mo partitioning data from Wade et al. (2012), which show significant scatter around our data and that of Wood et al. (2014), particularly at low S contents (see Figure S5 in the Supplementary Material). This scatter likely results from variations in melt polymerization and SiO_2 activity in their silicate melts, factors known to strongly influence W and Mo partitioning (Wade et al., 2012; Cottrell et al., 2009). These compositional effects obscure any potential influence of S on W and Mo partitioning between Fe-S liquid and silicate melt, leading us to exclude the data from Wade et al. (2012) from further consideration. We also do not include the sulfide melt–silicate melt partitioning data for Mo and Re from Feng and Li (2019), as their experiments were conducted under significantly more oxidizing conditions (FMQ −1.8 to FMQ +1.5) and used more andesitic compositions, which are less relevant to lunar mantle melting. We refer the reader to the study by Jennings et al. (2021), which, although not included in our literature comparison due to the absence of S-bearing experiments at 1.5 GPa, provides a comprehensive parameterization of Mo and W behavior in metal/silicate systems.

5.2 Implications of metal-saturation in the lunar mantle

The assumption that the lunar mantle is metal-saturated has clear implications to our understanding of the siderophile element abundances of lunar mare basalts. The presence of residual metal in the lunar mantle has already been used in the literature to explain the depletion of lunar samples in siderophile elements such as Re, Au, and Ge (e.g., Wolf and Anders, 1980). In order to assess the implications of metal-saturation in the lunar mantle, we performed aggregate modal fractional melting models assuming both different lunar bulk mantle compositions in equilibrium with a Fe-S liquid with ca. 10 wt% S. Part of the challenge in doing this is that most metal/silicate data refer to experiments carried out at much higher pressures and temperatures than those experienced even during lunar core formation, or especially, during partial melting of metal-saturated lunar mantle sources (1–2 GPa, 1200 °C; Charlier et al., 2018). Moreover, due to the high metal/silicate partition coefficients, most experiments involving HSE are doped with wt% levels of these elements to make it easier to measure their concentrations in silicate glasses. Because of this, the partitioning data obtained from these experiments is then corrected down to infinite dilution of HSE in an Fe-rich

metal alloy using available solution models (cf. Mann et al., 2012).

As shown in the previous subsection, this approach requires large extrapolations, and the corrected values do not necessarily reflect HSE behavior in natural metal/silicate systems. To avoid this, we use our own experimental partitioning data, minimizing HSE doping and covering P-T conditions relevant to lunar petrogenesis. We did not perform multivariate regression on our data, as commonly done (e.g., Righter, 2011), since such regressions would be under-constrained. The number of fitting parameters (four; related to enthalpy, entropy, molar volume, and S content of the metal) would exceed the number of observations (three to four experiments, depending on the element). To prevent inaccurate extrapolations, we used partitioning data from experiment L161, where the metal's S content (8.4 wt%) is closest to our estimate of 10 wt% S in the lunar residual metal phase.

To complement our Fe-S metal/silicate melt partitioning data, we incorporated literature data on equilibrium between lunar mantle silicates and an oxide (olivine, ortho- and clinopyroxene, ilmenite, plagioclase, and pigeonite) and silicate melt. Specifically, we used $D_{Mo,W}^{mineral/melt}$ data from Leitzke et al. (2017) and Dygert et al. (2013), as these studies focus on lunar mantle melting conditions. Notably, Leitzke et al. (2017) account for the decreasing incompatibility of W and Mo at lower lunar mantle fO_2. Similarly, we used mineral/melt partitioning data from Mallmann and O'Neill (2007) for Re, which – like Mo – becomes more tetravalent and less incompatible under reducing conditions. Following Brenan et al. (2019), we assume that Os, Ir, and Ru are compatible in olivine and orthopyroxene, while Pt and Pd remain incompatible. A summary of the partition coefficients and other compositional parameters used in our modeling are given in Table 6.

We considered several scenarios at a fixed degree of partial melting (10 %), consistent with mare basalt generation (Shearer et al., 2006). In the first scenario, a lunar mantle source composed of olivine and orthopyroxene in roughly equal proportions (50:50), corresponding to sequence 1 of the Lunar Magma Ocean (LMO) crystallization model of Snyder et al. (1992), and 0.1 % residual metal underwent partial melting. This model lunar mantle had bulk silicate Moon (BSM) trace element contents, with HSE abundances from Day et al. (2007, $\sim 0.0002 \times$ CI).

The Mo concentration in the lunar mantle is less well constrained. Newsom (1986) estimated lunar mantle depletion in Mo by a factor of 1200 relative to CI chondrites, yielding ca. 0.7 ng g^{-1} in BSM. Sharp et al. (2015), using their own metal-silicate partitioning data, estimated BSM Mo contents between 1 and 4 ng g^{-1} after lunar core formation. However, these low estimates lead to modeled Mo abundances in mare basalt melts that fall below measured values (gray line in Fig. 7; Newsom, 1986; Newsom and Maehr, 1993). To address this, we estimated the BSM Mo content by calculating how much Mo remained in a BSE-like lunar mantle, initially containing up to 180 ng g^{-1} Mo (Liang et al., 2017), after lunar core formation. Assuming a core fraction of 1.5 % (Weber et al., 2011) and using a $D_{Mo}^{metal/sil}$ of 338 (from an experiment at 4.5 GPa and 1900 °C), mass balance yielded $[Mo]_{BSM} = 29.7 \pm 5.8$ ng g^{-1}. The BSE Mo estimate by Liang et al. (2017) is on the higher end of published values, with the average being 47 ± 40 ng g^{-1} (Palme and O'Neill, 2014). However, Liang et al. (2017) argue that Mo behaves more compatibly during partial melting than previously assumed, which past BSE estimates may not account for. Since earlier BSM Mo estimates rely on these BSE values, we suggest they underestimate the true lunar mantle Mo content, agreeing with Leitzke et al. (2017). Thus, we adopt our own estimate of 29.7 ± 5.8 ng g^{-1} based on Liang et al. (2017) and our lunar core formation-relevant $D_{Mo}^{metal/sil}$. Applying the same approach to W, using an initial BSE value of 12 ng g^{-1} (König et al., 2011) and a $D_{W}^{metal/sil}$ of 12 ± 3, we obtained $[W]_{BSM} = 10.3 \pm 3.5$ ng g^{-1}, a factor of two lower than the 20 ng g^{-1} estimate by Münker (2010). However, given the differences in how both estimates were obtained – specifically, that Münker (2010) derived theirs from mass balance calculations based on high-precision isotope dilution trace element ratios, whereas we used a simpler mass balance approach relying on our $D_{W}^{metal/sil}$ and an assumed core fraction of 1.5 wt% – we consider both estimates to be reasonably close.

The 10 % fractional melting model closely reproduces the observed mare basalt HSE, W, and Mo concentrations and overall pattern (full blue line in Fig. 7a). In contrast, assuming a metal-saturated BSE-like lunar mantle without accounting for lunar core formation (shaded blue line in Fig. 7a) results in HSE values far exceeding those in the mare basalt record. This suggests that the HSE estimate by Day et al. (2007) accurately reflects lunar mantle abundances after core formation. An alternative model incorporating a hybrid lunar mantle composition – 70 % ultramafic cumulates from sequence 1 and 30 % ilmenite-bearing cumulates from sequence 5 of Snyder et al. (1992) – represents a mixed lunar source that could have formed after mantle overturn. This model yields a similar outcome, albeit with slightly higher HSE contents (Fig. 7a), compared to a source composed solely of olivine and orthopyroxene.

Broader variations in HSE, Mo, and W contents in the modeled basalts arise from changes in the metal content of the source (Figure 7b). As expected, a source with minimal residual Fe-S metal (250 µg g^{-1}) produces the highest HSE, Mo, and W concentrations in 10 % partial melts. In contrast, a lunar mantle source with 1 wt% Fe-S metal would be more depleted in most elements compared to the mare basalt record. These results align well with lunar mantle S estimates ($\sim$80 µg g^{-1} S; Hauri et al., 2015), which, as noted earlier, correspond to a metal fraction of 0.05–0.1 wt% in the lunar mantle – depending on the exact Ni and S contents of the metal phase – assuming all sulfur resides in the residual metal. Comparatively, lower degree partial melts yield little variation in their HSE and Mo contents, with only W being affected. This is unsurprising given that W is the only element that shows an overall incompatible bulk partitioning behavior, whereas the HSE and Mo are purely compatible. Please refer to the Supporting Data where a

Table 6. List of mineral/melt partition coefficients used in the modeling of fractional melting of high Mg mare basalt sources. Modal abundances taken from Snyder et al. (1992). Data sources for partitioning data: Bre19 – Brenan et al. (2019); Day07 – Day et al. (2007); Dyg13 - Dygert et al. (2013); Kön11 – König et al. (2011); Lia17 – Liang et al. (2017); Lei17 – Leitzke et al. (2017); Mal07 – Mallmann and O'Neill (2007); Pal14 – Palme and O'Neill (2014); Thi19 – Thiemens et al. (2019). All metal/silicate melt partitioning data used are taken from Experiment L161 (see text for discussion). *Assumed that BSM has 30 ng g^{-1} Mo. This value was calculated assuming segregation of 1.5 wt% core material from an initially BSE-like lunar mantle that originally had 180 ng g^{-1} Mo (after Liang et al., 2017). Partitioning data from experiment E398 were used for to calculate the Mo content of the lunar mantle post lunar core formation.

Modal abundances			Mineral/melt partition coefficients							
Mineral	Ultramafic	Hybrid	Os	Ir	Ru	Pt	Pd	Re	Mo	W
Olivine	0.509	0.36	3	3	3	0.001	0.001	0.09	0.47	0.005
Orthopyroxene	0.49	0.343	3	3	3	0.001	0.001	0.9	0.72	0.006
Clinopyroxene		0.072	n/a	n/a	n/a	n/a	n/a	2	2.18	0.047
Pigeonite		0.102	n/a	n/a	n/a	n/a	n/a	1.2	0.72	0.006
Plagioclase		0.093	n/a	n/a	n/a	n/a	n/a	n/a	0.4	0.0006
Ilmenite		0.033	n/a	n/a	n/a	n/a	n/a	0.97	5.91	0.075
Fe-S metal	0.001	0.0007	18000	33000	22000	11000	16000	5700	323	15
Data sources			**Os**	**Ir**	**Ru**	**Pt**	**Pd**	**Re**	**Mo**	**W**
Silicates			Bre19	Bre19	Bre19	Bre19	Bre19	Mal07	Lei17	Lei17
Oxides			n/a	n/a	n/a	n/a	n/a	n/a	Lei17	Dyg13
BSE			Pal14	Pal14	Pal14	Pal14	Pal14	Pal14	Lia17	Kön11
BSM			Day07	Day07	Day07	Day07	Day07	Day07	Lia17*	Thi19

spreadsheet showing how the partial melting models are calculated is included (Fonseca et al., 2026).

Despite differences in their elevated $D_i^{met/sil}$, Re and Os are only slightly fractionated during partial melting of the lunar mantle in our models. Consequently, some radiogenic ingrowth of ^{187}Os is expected in mare basalts derived from a metal-saturated lunar mantle source. Assuming that the lunar mantle had a CI chondritic initial Os isotope composition (i.e., $[^{187}Re/^{188}Os]_i$ of 0.42, $[^{187}Os/^{188}Os]_i$ of 0.0961; Fischer-Gödde et al., 2010), it would have evolved to $^{187}Re/^{188}Os$ values of 0.1212 and 0.115 by 3.0 and 3.9 Ga, respectively (using a decay constant λ of 1.66×10^{-11} a^{-1}; Smoliar et al., 1996). An Fe-S metal-saturated silicate melt formed at those times would have a Re/Os of approximately 0.28 (or $^{187}Re/^{188}Os$ of 1.31), based on our metal/silicate partitioning data for Re and Os ($D_{Re}^{metal/sil}/D_{Os}^{metal/sil} \sim 0.27$). Such melts would develop $^{187}Os/^{188}Os$ values of 0.188 and 0.199 between 3.0 and 3.9 Ga. These values are consistent with the overall suprachondritic Os isotope compositions observed in Apollo 12, 15, and 17 mare basalts, even though most lunar samples show near-chondritic or slightly suprachondritic values (Day et al., 2007; Day and Walker, 2015). Our calculated Os isotope compositions are slightly higher than the present-day maximum observed $^{187}Os/^{188}Os$ of 0.18 (see Figure 2 of Day, 2018). This suggests that regolith assimilation is required to bring $^{187}Os/^{188}Os$ values down to near-chondritic levels, as proposed by Brenan et al. (2019). Variable assimilation of chondritic regolith, combined with differences in residual metal fractions in lunar mantle sources, can explain both the observed spread in $^{187}Os/^{188}Os$ and the elevated HSE abundances in lunar rocks, which often exceed those predicted by our partial melting models. However, due to very low Re and Os concentrations in the quenched silicate melts from our experiments, $D_{Re}^{metal/sil}$ and, to a lesser extent, $D_{Os}^{metal/sil}$, remain imprecisely determined. This results in up to 45 % variation in the calculated $^{187}Os/^{188}Os$, yielding a range from 0.102 to 0.276, spanning both sub- and suprachondritic values. Thus, while our average $D_{Re,Os}^{metal/sil}$ values support the generation of suprachondritic melts, the associated uncertainties do not exclude the possibility of subchondritic compositions. Moreover, it remains unclear whether lunar core formation significantly fractionated Re/Os. If so, the lunar mantle may have acquired a non-chondritic Re/Os ratio, further complicating accurate estimates of the Os isotopic composition in parental mare basaltic melts.

5.3 Could residual metal be a remnant of core formation?

Weber et al. (2011) have argued, based on a re-evaluation of seismic data obtained during the Apollo missions, that the Moon has a small metallic core with up to 3 % of the mass of the Moon. Irrespective of whether one assumes metal or sulfide saturation in lunar mantle sources, the fact that the Moon has a metallic core must have resulted in the depletion of siderophile elements from the silicate Moon. Complementarily, lunar core formation is also supported by geochemical data. Burkhardt et al. (2014) showed that lunar mare basalts are enriched in heavy Mo isotopes, which is consistent with Mo isotope equilibrium stable isotope fractionation during high-temperature core formation (up to 3000 °C; see Hin et al., 2013). More recently, Xia et al. (2019) have carried out metal-silicate equilibrium

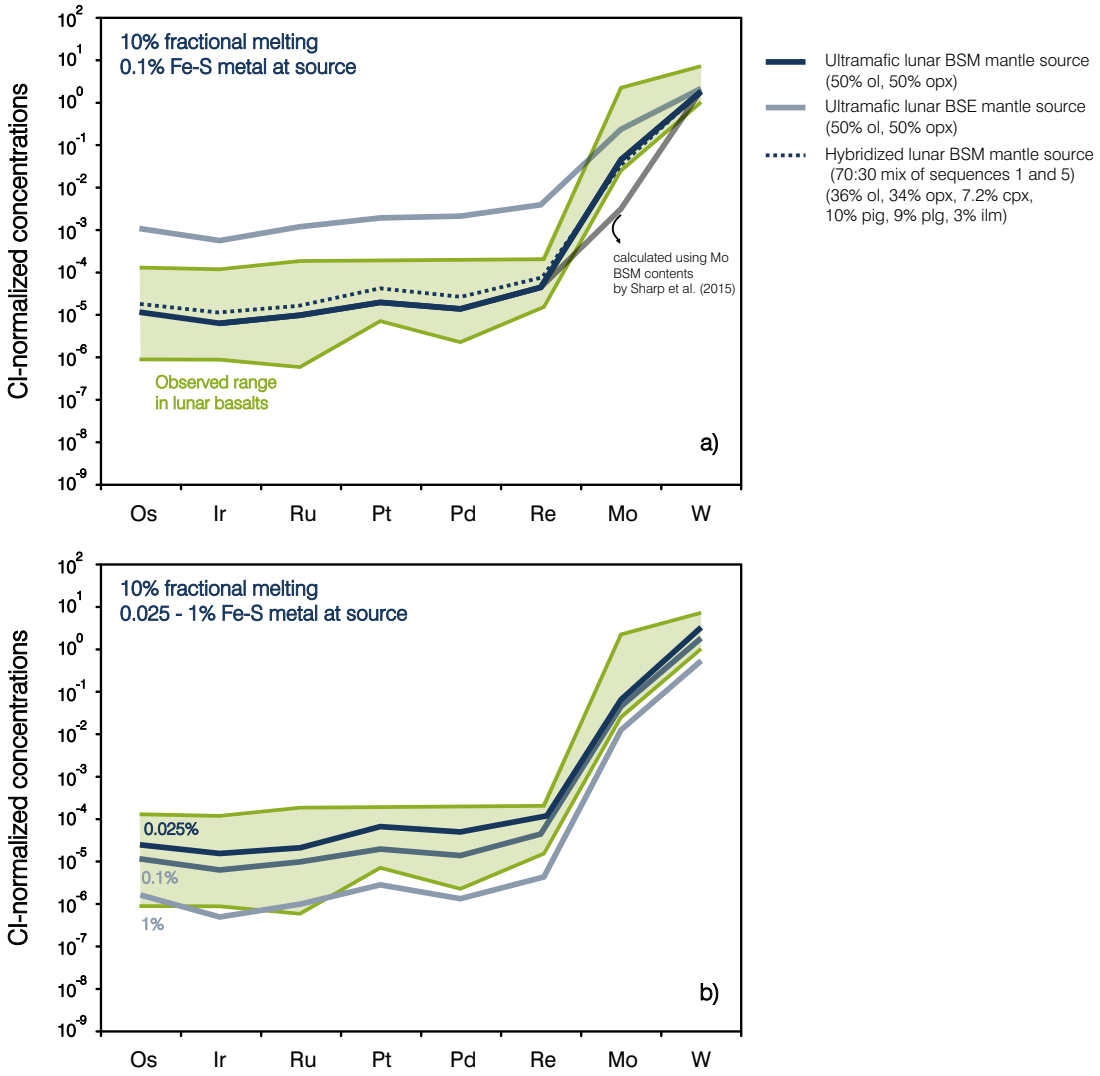

Figure 7. Modeled HSE, Mo and W abundances of lunar mare basalts that result from 10 % fractional melting of a BSE-like and BSM-like lunar mantle sources that contain 0.1 % Fe-rich metal. The observed range of concentrations seen in natural lunar mare basalts are taken from Day and Walker (2015); Newsom (1986); Newson (1995); Thiemens et al. (2019); O'Neill (1991)

experiments and showed that the Cu isotope composition of the silicate Moon is consistent with the sequestration of Cu into the lunar core, although it should be noted that their assumption of a pure FeS lunar core in most of their experiments is perhaps not fully representative of lunar core formation. Finally, lunar core formation has been shown to easily account for the moderately siderophile element abundances of lunar mare basalts (Rai and van Westrenen, 2014), and is a function of temperature and assumed core sulfur content (Steenstra et al., 2016, 2020).

The Moon's small size suggests that core segregation may have been incomplete, similar to observations in some achondrites displaying incomplete metal segregation (Elkins-Tanton and Weiss, 2017). However, full crystallization of the LMO could have occurred over 150–200 million years after solar system formation (Borg et al., 2011, 2019; Maurice et al., 2020). This extended timescale could facilitate complete metal segregation into the lunar core, especially in the context of a global LMO (Borg et al., 2011). Recent arguments by Steenstra et al. (2020) support a high-temperature origin for the Moon, potentially from a giant impact, and a global LMO. Nevertheless, conflicting studies suggest that KREEP crystallization, assumed to mark the final stages of the LMO, occurred much earlier, around 4.43 to 4.51 billion years ago (Münker, 2010; Thiemens et al., 2019; Greer et al., 2023; Nimmo et al., 2024; Dauphas et al., 2025; Barboni et al., 2017). Additionally, Charlier et al. (2018) proposed that the thin lunar crust indicates a shallower LMO than previously thought, cooling over a shorter period and hindering complete core segregation. Efficient Fe-FeS metal segregation in a solid lunar mantle would likely require a minimum of 5 vol% of liquid metal (Yoshino et al., 2003; Ballhaus and Ellis, 1996; Holzheid et al., 2000; Terasaki et al., 2008). However, the small volume fraction of the lunar core and the high dihedral wetting angle of Fe-S melts ($\Theta \sim 80$–$100°$) suggest that the segregation threshold may not be reached in a solid lunar mantle (Ghanbarzadeh et al., 2017; Duncan and Fei, 2017). It is important to consider that most LMO crystallization models assume a small fraction (1–3 %) of

trapped interstitial silicate liquid in various LMO cumulates (Snyder et al., 1992; Sprung et al., 2013; Fonseca et al., 2014). However, Holzheid et al. (2000) noted that adding silicate melt to a solid olivine-rich matrix minimally affects the dihedral angle for Fe-S liquid. As such the presence of trapped interstitial silicate melt is unlikely to have facilitated efficient core segregation. Moreover, silicate melts wet mineral surfaces far more effectively than metallic melts. Consequently, if silicate melts were trapped, it is also likely that a small fraction of Fe-S metallic melt was retained within lunar mantle cumulates.

The question arises: could a portion of core metal have remained trapped in the lunar mantle after LMO solidification? This idea is appealing, suggesting that the lunar mantle might retain some siderophile elements that would otherwise be transferred entirely to the lunar core. However, the ongoing debate over the Moon's age and the timescale of LMO crystallization leaves the issue of whether the presumably metal-saturated lunar mantle is a by-product of incomplete core segregation open to discussion. The extent to which such liquids may segregate in more complex mineral matrices remains poorly understood. Most studies have focused on the segregation of metallic melts in monomineralic matrices like olivine (e.g., Gaetani and Grove, 1999; Berg et al., 2017, 2018; Terasaki et al., 2008; Ghanbarzadeh et al., 2017), or used proxies like hexagonal boron nitride (h-BN) and MgO (Berg et al., 2018). Indeed, Beyer et al. (2024) have recently shown that Fe-S melt migration in polymineralic matrices is more complex than previously assumed, and that the migration threshold for Fe-S liquids is fairly matrix-dependent. The role of oxides, particularly in ilmenite-bearing cumulates presumed to have crystallized from the LMO, has not been thoroughly explored, except for a single study by Brenan and Rose (2002) on the mobility of sulfide liquids in a solid chromite matrix. This study found that sulfide melts exhibit dihedral angles in chromite grain surfaces below the segregation threshold of 60°. If applicable to ilmenite-bearing cumulates, it suggests that lunar core melts may have been mobile in some LMO cumulates but not in others. Further investigation is needed to explore these possibilities beyond speculation.

6 Conclusions

The geochemical and petrological characteristics of lunar mare basalts are consistent with their formation by partial melting of a lunar mantle that is metal-saturated. This raised the initial question of whether the fO_2 values derived from lunar basalts are truly representative of their sources. If the widely accepted estimate of the lunar mantle's fO_2 at IW −1 is correct, which we argued earlier that it is, then equilibrium thermodynamics dictates that the mantle sources of both low- and high-Ti basalts must indeed have been metal-saturated. Our modeling, coupled with partitioning data, supports this conclusion, demonstrating that partial melting of a lunar mantle with BSM-like siderophile element contents can account for the observed range of HSE, Mo, and W abundances in lunar mare basalts, provided that the mantle contains approximately 0.1 wt% of Fe-S residual metal. Importantly, our data show that W abundances in lunar basalts are not reliable indicators of residual metal in lunar mantle sources, as W remains incompatible and exhibits low metal/silicate partitioning under lunar mantle melting conditions.

The composition of this residual metal is also a key consideration and a key question surrounding the possibility of metal saturation of the lunar mantle. Our results suggest that it likely contains around 10 wt% S, a value in agreement with previous experimental studies (cf. Brenan et al., 2019) and with estimates of the sulfur content of the lunar mantle (70–160 $\mu g\, g^{-1}$; cf. Chen et al., 2015; Hauri et al., 2015). However, the presence of residual metal in lunar mantle sources has broader implications, particularly regarding the interplay between metal saturation and lunar core formation. Given that core formation is expected to deplete the mantle in siderophile elements, reconciling this process with a metal-saturated mantle presents a challenge. If both processes had acted in full, lunar mare basalts would likely be far more depleted in siderophile elements than they appear to be. To resolve this, we propose that the residual metal in the lunar mantle represents a remnant of incomplete core formation. If the lunar magma ocean crystallized rapidly, a small fraction of core melts may have failed to efficiently percolate through the increasingly solidified mantle cumulates, resulting in their partial retention as a pinched-off core melt fraction.

Acknowledgements

We are grateful to Ralf Dohmen and Chris Ballhaus for discussions that helped shape the manuscript. Nils Jöns and René Hoffmann are thanked for their support during electron microprobe and SEM measurements. We thank two anonymous reviewers for their constructive feedback that greatly improved this manuscript. ROCF is grateful for financial support from the Deutsche Forschungsgemeinschaft (via grant number FO 698/13–1).

Data, code, and outputs availability

Supplementary Figures S1–S5 are available in the accompanying Supplementary Material. All acquired raw data, partial melting models and fO_2 calculations are available in the Zenodo open data repository of Fonseca et al. (2026, https://doi.org/10.5281/zenodo.20525326). Main text figures and tables are available for download in the online version of this article.

Competing interests

The authors declare no competing interests.

Licence agreement

This article is distributed under the terms of the Creative Commons Attribution 4.0 International Licence (CC BY

4.0), which permits unrestricted use, distribution, and reproduction in any medium, provided appropriate credit is given to the original author(s) and source, as well as a link to the Creative Commons licence, and an indication of changes that were made.

References

Adam J, Green T (2006). Trace element partitioning between mica-and amphibole-bearing garnet lherzolite and hydrous basanitic melt: 1. Experimental results and the investigation of controls on partitioning behaviour. *Contributions to Mineralogy and Petrology* 152: 1–17. doi:10.1007/s00410-006-0085-4

Ballhaus C, Ellis DJ (1996). Mobility of core melts during Earth's accretion. *Earth and Planetary Science Letters* 143(1-4): 137–145. doi:10.1016/0012-821X(96)00135-5

Ballhaus C, Leitzke FP, Fonseca ROC, Nagel T, Kuzmin D, El Goresy A (2022). Metal Saturated Cumulates from Siberia—Lunar Basalt Analogues? *Journal of Petrology* 63(8): egac067. doi:10.1093/petrology/egac067

Barboni M, Boehnke P, Keller B, Kohl IE, Schoene B, Young ED, McKeegan KD (2017). Early formation of the Moon 4.51 billion years ago. *Science Advances* 3: e1602365. doi:10.1126/sciadv.1602365

Barin I (1995). *Thermochemical Data of Pure Substances*. VCH, Weinheim, Germany; New York, NY, USA, 3rd edn. doi:10.1002/9783527619825

Berg MT, Bromiley GD, Butler IB, Frost M, Bradley R, Carr J, Le Godec Y, Montési LG, Zhu W, Miller K, et al. (2017). Deformation-aided segregation of Fe-S liquid from olivine under deep Earth conditions: Implications for core formation in the early solar system. *Physics of the Earth and Planetary Interiors* 263: 38–54. doi:10.1016/j.pepi.2017.01.004

Berg MTL, Bromiley GD, Le Godec Y, Philippe J, Mezouar M, Perrillat JP, Potts NJ (2018). Rapid Core Formation in Terrestrial Planets by Percolative Flow: In-Situ Imaging of Metallic Melt Migration Under High Pressure/Temperature Conditions. *Frontiers in Earth Science* 6: 77. doi:10.3389/feart.2018.00077

Beyer C, Fonseca R, Bissbort T, Schröer L, Cnudde V (2024). Sulfide melt wetting properties in Earth's mantle: New constraints from combined 2D and 3D imaging. *Geochemistry, Geophysics, Geosystems* 25(5): e2024GC011535. doi:10.1029/2024GC011535

Beyer C, Myhill R, Marquardt K, McCammon CA (2021). A reversed redox gradient in Earth's mantle transition zone. *Earth and Planetary Science Letters* 575: 117181. doi:10.1016/j.epsl.2021.117181

Borg LE, Connelly JN, Boyet M, Carlson RW (2011). Chronological evidence that the Moon is either young or did not have a global magma ocean. *Nature* 477(7362): 70. doi:10.1038/nature10328

Borg LE, Gaffney AM, Kruijer TS, Marks NA, Sio CK, Wimpenny J (2019). Isotopic evidence for a young lunar magma ocean. *Earth and Planetary Science Letters* 523. doi:10.1016/j.epsl.2019.07.008

Brenan JM, Mungall JE, Bennett NR (2019). Abundance of highly siderophile elements in lunar basalts controlled by iron sulfide melt. *Nature Geoscience* 12(9): 701–706. doi:10.1038/s41561-019-0426-3

Brenan JM, Rose LA (2002). Experimental constraints on the wetting of chromite by sulfide liquid. *The Canadian Mineralogist* 40(4): 1113–1126. doi:10.2113/gscanmin.40.4.1113

Buono AS, Walker D (2011). The Fe-rich liquidus in the Fe–FeS system from 1 bar to 10 GPa. *Geochimica et Cosmochimica Acta* 75(8): 2072–2087. doi:10.1016/j.gca.2011.01.030

Burkhardt C, Hin RC, Kleine T, Bourdon B (2014). Evidence for Mo isotope fractionation in the solar nebula and during planetary differentiation. *Earth and Planetary Science Letters* 391: 201–211. doi:10.1016/j.epsl.2014.01.037

Chabot NL, Campbell AJ, Jones JH, Humayun M, Agee CB (2003). An experimental test of Henry's Law in solid metal-liquid metal systems with implications for iron meteorites. *Meteoritics & Planetary Science* 38(2): 181–196. doi:10.1111/j.1945-5100.2003.tb00259.x

Charlier B, Grove TL, Namur O, Holtz F (2018). Crystallization of the lunar magma ocean and the primordial mantle-crust differentiation of the Moon. *Geochimica et Cosmochimica Acta* 234: 50–69. doi:10.1016/j.gca.2018.05.006

Chen Y, Zhang Y, Liu Y, Guan Y, Eiler J, Stolper EM (2015). Water, fluorine, and sulfur concentrations in the lunar mantle. *Earth and Planetary Science Letters* 427: 37–46. doi:10.1016/j.epsl.2015.06.046

Cottrell E, Walter M, Walker D (2009). Metal-silicate partitioning of tungsten at high pressure and temperature: Implications for equilibrium core formation in Earth. *Earth and Planetary Science Letters* 281(3-4): 275–287. doi:10.1016/j.epsl.2009.02.024

Crocket JH, Fleet ME, Stone WE (1997). Implications of composition for experimental partitioning of platinum-group elements and gold between sulfide liquid and basalt melt: The significance of nickel content. *Geochimica et Cosmochimica Acta* 61(19): 4139–4149. doi:10.1016/S0016-7037(97)00234-2

Danielson LR, Righter K, Newville M, Sutton S, Choi Y, Pando K (2011). Molybdenum valence in basaltic silicate melts: Effects of temperature and pressure. In *Lunar and Planetary Science Conference Proceedings*, vol. 42, p. 2609. bibcode:2011LPI....42.2609D

Dauphas N, Zhang ZJ, Chen X, Barboni M, Szymanowski D, Schoene B, Leya I, McKeegan KD (2025). Completion of lunar magma ocean solidification at 4.43 Ga. *Proceedings of the National Academy of Sciences* 122(2): e2413802121. doi:10.1073/pnas.2413802121

Day JM, Paquet M (2021). Temporally limited late accretion after core formation in the Moon. *Meteoritics & Planetary Science* 56(4): 683–699. doi:10.1111/maps.13646

Day JM, Pearson DG, Taylor LA (2007). Highly siderophile element constraints on accretion and differentiation of the Earth-Moon system. *Science* 315(5809): 217–219. doi:10.1126/science.1133355

Day JMD (2018). Geochemical constraints on residual metal and sulfide in the sources of lunar mare basalts. *American Mineralogist: Journal of Earth and Planetary Materials* 103(11): 1734–1740. doi:10.2138/am-2018-6368

Day JMD, Walker RJ (2015). Highly siderophile element depletion in the Moon. *Earth and Planetary Science Letters* 423: 114–124. doi:10.1016/j.epsl.2015.05.001

Delano JW (1990). Experimental constraints on the oxidation state of the lunar mantle. In *Lunar and Planetary Science Conference Proceedings*, vol. 21, pp. 278–279. bibcode:1990LPI....21..278D

DesMarais DJ, Hayes JM, Meinschein WG (1974). Retention of solar wind-implanted elements in lunar soils. In *Lunar and Planetary Science Conference*, vol. 5, pp. 168–170. bibcode:1974LPI.....5..168D

Dickey Jr JS (1970). Nickel-iron in lunar anorthosites. *Earth and Planetary Science Letters* 8(6): 387–392. doi:10.1016/0012-821X(70)90140-8

Ding S, Hough T, Dasgupta R (2018). New high pressure experiments on sulfide saturation of high-FeO* basalts with variable TiO_2 contents–Implications for the sulfur inventory of the lunar interior. *Geochimica et Cosmochimica Acta* 222: 319–339. doi:10.1016/j.gca.2017.10.025

Duncan MS, Fei Y (2017). Experimental constraints on metal percolation through silicate: implications for core formation on asteroids and planetesimals. In *Lunar and Planetary Science Conference Proceedings*, vol. 48, p. 1505. bibcode:2017LPI....48.1505D

Dungan MA, Brown RW (1977). The petrology of the Apollo 12 ilmenite basalt suite. *Lunar Science Conference Proceedings* 8: 1339–1381. bibcode:1977LPSC....8.1339D

Dygert N, Liang Y, Hess P (2013). The importance of melt TiO_2 in affecting major and trace element partitioning between Fe–Ti oxides and lunar picritic glass melts. *Geochimica et Cosmochimica Acta* 106: 134–151. doi:10.1016/j.gca.2012.12.005

Elkins-Tanton LT, Weiss BP (eds.) (2017). *Planetesimals: early differentiation and consequences for planets*. Cambridge University Press. doi:10.1017/9781316339794

Farrell WM, Hurley DM, Zimmerman MI (2015). Solar wind implantation into lunar regolith: Hydrogen retention in a surface with defects. *Icarus* 255: 116–126. doi:10.1016/j.icarus.2014.09.014

Feng L, Li Y (2019). Comparative partitioning of Re and Mo between sulfide phases and silicate melt and implications for the behavior of Re during magmatic processes. *Earth and Planetary Science Letters* 517: 14–25. doi:10.1016/j.epsl.2019.04.010

Fischer-Gödde M, Becker H, Wombacher F (2010). Rhodium, gold and other highly siderophile element abundances in chondritic meteorites. *Geochimica et Cosmochimica Acta* 74(1): 356–379. doi:10.1016/j.gca.2009.09.024

Fleet ME, Crocket JH, Menghua L, Stone WE (1999). Laboratory partitioning of platinum-group elements (PGE) and gold with applications to magmatic sulfide-PGE deposits. *Lithos* 47: 127–142. doi:10.1016/S0024-4937(99)00011-0

Fonseca ROC, Beyer C, Bissbort T, Hartmann R, Schuth S (2024). Partitioning of highly siderophile elements between monosulfide solid solution and sulfide melt at high pressures. *Contributions to Mineralogy and Petrology* 179(2): 1–17. doi:10.1007/s00410-023-02092-y

Fonseca ROC, Beyer C, Schuth S, Leitzke F (2026). Metal saturation experiments and compositional modelling for the lunar mantle. Version v7. Zenodo. doi:10.5281/zenodo.20525326

Fonseca ROC, Brückel K, Bragagni A, Leitzke FP, Speelmanns IM, Wainwright AN (2017). Fractionation of rhenium from osmium during noble metal alloy formation in association with sulfides: Implications for the interpretation of model ages in alloy-bearing magmatic rocks. *Geochimica et Cosmochimica Acta* 216: 184–200. doi:10.1016/j.gca.2017.04.041

Fonseca ROC, Mallmann G, Sprung P, Sommer JE, Heuser A, Speelmanns IM, Blanchard H (2014). Redox controls on tungsten and uranium crystal/silicate melt partitioning and implications for the U/W and Th/W ratio of the lunar mantle. *Earth and Planetary Science Letters* 404: 1–13. doi:10.1016/j.epsl.2014.07.015

Gaetani GA, Grove TL (1999). Wetting of mantle olivine by sulfide melt: implications for Re/Os ratios in mantle peridotite and late-stage core formation. *Earth and Planetary Science Letters* 169: 147–163. doi:10.1016/S0012-821X(99)00062-X

Gaillard F, Scaillet B, Arndt NT (2011). Atmospheric oxygenation caused by a change in volcanic degassing pressure. *Nature* 478(7368): 229–232. doi:10.1038/nature10460

Ghanbarzadeh S, Hesse MA, Prodanović M (2017). Percolative core formation in planetesimals enabled by hysteresis in metal connectivity. *Proceedings of the National Academy of Sciences* 114(51): 13406–13411. doi:10.1073/pnas.1707580114

Greer J, Zhang B, Isheim D, Seidman DN, Bouvier A, Heck PR (2023). 4.46 Ga zircons anchor chronology of lunar magma ocean. *Geochemical Perspectives Letters* 27: 49–53. doi:10.7185/geochemlet.2334

Hauri EH, Saal AE, Rutherford MJ, Van Orman JA (2015). Water in the Moon's interior: Truth and consequences. *Earth and Planetary Science Letters* 409: 252–264. doi:10.1016/j.epsl.2014.10.053

Hernlund J, Leinenweber K, Locke D, Tyburczy JA (2006). A numerical model for steady-state temperature distributions in solid-medium high-pressure cell assemblies. *American Mineralogist* 91(2-3): 295–305. doi:10.2138/am.2006.1938

Hin RC, Burkhardt C, Schmidt MW, Bourdon B, Kleine T (2013). Experimental evidence for Mo isotope fractionation between metal and silicate liquids. *Earth and Planetary Science Letters* 379: 38–48. doi:10.1016/j.epsl.2013.08.003

Holzheid A, Borisov A, Palme H (1994). The effect of oxygen fugacity and temperature on solubilities of nickel, cobalt, and molybdenum in silicate melts. *Geochimica et Cosmochimica Acta* 58(8): 1975–1981. doi:10.1016/0016-7037(94)90429-4

Holzheid A, Palme H, Chakraborty S (1997). The activities of NiO, CoO and FeO in silicate melts. *Chemical Geology* 139(1-4): 21–38. doi:10.1016/S0009-2541(97)00030-2

Holzheid A, Schmitz MD, Grove TL (2000). Textural equilibria of iron sulfide liquids in partly molten silicate aggregates and their relevance to core formation scenarios. *Journal of Geophysical Research: Solid Earth* 105(B6): 13555–13567. doi:10.1029/2000JB900046

Jennings ES, Jacobson SA, Rubie DC, Nakajima Y, Vogel AK, Rose-Weston L, Frost DJ (2021). Metal–silicate partitioning of W and Mo and the role of carbon in controlling their abundances in the bulk silicate earth. *Geochimica et Cosmochimica Acta* 293: 40–69. doi:10.1016/j.gca.2020.09.035

Jochum KP, Weis U, Stoll B, Kuzmin D, Yang Q, Raczek I, Jacob DE, Stracke A, Birbaum K, Frick DA, et al. (2011). Determination of reference values for NIST SRM 610–617 glasses following ISO guidelines. *Geost Geoanal Res* 35: 397–429. doi:10.1111/j.1751-908x.2011.00120.x

Jones JH (2004). Redox conditions among the terrestrial planets. In *Lunar and Planetary Science Conference Proceedings*, vol. 35, p. 1264. bibcode:2004LPI....35.1264J

Karner J, Papike J, Shearer C (2003). Olivine from planetary basalts: Chemical signatures that indicate planetary parentage and those that record igneous setting and process. *American Mineralogist* 88: 806–816. doi:10.2138/am-2003-5-609

Karner JM, Sutton SR, Papike JJ, Shearer CK, Jones JH, Newville M (2006). Application of a new vanadium valence oxybarometer to basaltic glasses from the Earth, Moon, and Mars. *American Mineralogist* 91(2-3): 270–277. doi:10.2138/am.2006.1830

König S, Münker C, Hohl S, Paulick H, Barth A, Lagos M, Pfänder J, Büchl A (2011). The Earth's tungsten budget during mantle melting and crust formation. *Geochimica et Cosmochimica Acta* 75(8): 2119–2136. doi:10.1016/j.gca.2011.01.031

Laurenz V, Rubie DC, Frost DJ, Vogel AK (2016). The importance of sulfur for the behavior of highly-siderophile elements during Earth's differentiation. *Geochimica et Cosmochimica Acta* 194: 123–138. doi:10.1016/j.gca.2016.08.012

Leitzke FL, Fonseca ROC, Michely LT, Sprung P, Münker C, Heuser A, Blanchard H (2016). The effect of titanium on the partitioning behavior of high-field strength elements between silicates, oxides and lunar basaltic melts with applications to the origin of mare basalts. *Chemical Geology* 440: 219–238. doi:10.1016/j.chemgeo.2016.07.011

Leitzke FP, Fonseca ROC, Göttlicher J, Steininger R, Jahn S, Prescher C, Lagos M (2018). Ti K-edge XANES study on the coordination number and oxidation state of Titanium in pyroxene, olivine, armalcolite, ilmenite, and silicate glass during mare basalt petrogenesis. *Contributions to Mineralogy and Petrology* 173(12): 103. doi:10.1007/s00410-018-1533-7

Leitzke FP, Fonseca ROC, Sprung P, Mallmann G, Lagos M, Michely LT, Münker C (2017). Redox dependent behaviour of molybdenum during magmatic processes in the terrestrial and lunar mantles: Implications for the Mo/W of the bulk silicate Moon. *Earth and Planetary Science Letters* 474: 503–515. doi:10.1016/j.epsl.2017.07.009

Li C, Ripley EM, Mathez EA (2003). The effect of S on the partitioning of Ni between olivine and silicate melt in MORB. *Chemical Geology* 201(3-4): 295–306. doi:10.1016/j.chemgeo.2003.08.008

Liang YH, Halliday AN, Siebert C, Fitton JG, Burton KW, Wang KL, Harvey J (2017). Molybdenum isotope fractionation in the mantle. *Geochimica et Cosmochimica Acta* 199: 91–111. doi:10.1016/j.gca.2016.11.023

Longerich HP, Jackson SE, Günther D (1996). Laser ablation inductively coupled plasma mass spectrometric transient signal data acquisition and analyte concentration calculation. *J Anal At Spectrom* 11: 899–904. doi:10.1039/ja9961100899

Mallmann G, O'Neill HSC (2007). The effect of oxygen fugacity on the partitioning of rhenium between crystals and silicate melt during mantle melting. *Geochimica et Cosmochimica Acta* 71(11): 2837–2857. doi:10.1016/j.gca.2007.03.028

Mallmann G, O'Neill HSC (2009). The crystal/melt partitioning of V during mantle melting as a funtion of oxygen fugacity compared with some other elements (Al, P, Ca, Sc, Ti, Cr, Fe, Ga, Y, Zr and Nb. *Journal of Petrology* 50: 1765–1794. doi:10.1093/petrology/egp053

Mann U, Frost DJ, Rubie DC, Becker H, Audétat A (2012). Partitioning of Ru, Rh, Pd, Re, Ir and Pt between liquid metal and silicate at high pressures and high temperatures-Implications for the origin of highly siderophile element concentrations in the Earth's mantle. *Geochimica et Cosmochimica Acta* 84: 593–613. doi:10.1016/j.gca.2012.01.026

Maruyama N, Ban-Ya S (1978). Measurement of Activities in Liquid Fe–Ni, Fe–Co and Ni–Co Alloys by a Transportation Method. *Journal of the Japan Institute of Metals* 42(10): 992–999. doi:10.2320/jinstmet1952.42.10_992

Maurice M, Tosi N, Schwinger S, Breuer D, Kleine T (2020). A long-lived magma ocean on a young Moon. *Science advances* 6(28): eaba8949. doi:10.1126/sciadv.aba8949

Mavrogenes JA, O'Neill HSC (1999). The relative effects of pressure, temperature and oxygen fugacity on the solubility of sulfide in mafic magmas. *Geochimica et Cosmochimica Acta* 73: 1173–1180. doi:10.1016/S0016-7037(98)00289-0

Métrich N, Berry AJ, O'Neill HSC, Susini J (2009). The oxidation state of sulfur in synthetic and natural glasses determined by X-ray absorption spectroscopy. *Geochimica et Cosmochimica Acta* 73(8): 2382–2399. doi:10.1016/j.gca.2009.01.025

Meyer C (2010). Lunar Sample Compendium. In *Lunar and Planetary Science Conference Proceedings*, vol. 41, p. 1016. bibcode:2010LPI....41.1016M

Moore CB, Lewis CF, Gibson Jr EK (1973). Total carbon contents of Apollo 15 and 16 lunar samples. In *Lunar and Planetary Science Conference Proceedings*, vol. 4, pp. 1613–1623. bibcode:1973LPSC....4.1613M

Moore JG, Schilling JG (1973). Vesicles, water, and sulfur in Reykjanes Ridge basalts. *Contributions to Mineralogy and Petrology* 41(2): 105–118. doi:10.1007/BF00375036

Münker C (2010). A high field strength element perspective on early lunar differentiation. *Geochimica et Cosmochimica Acta* 74(24): 7340–7361. doi:10.1016/j.gca.2010.09.021

Newsom HE (1986). Constraints on the origin of the Moon from the abundance of molybdenum and other siderophile elements. In *Origin of the Moon; Proceedings of the Conference, Kona, HI*, pp. 203–229. bibcode:1986ormo.conf..203N

Newsom HE, Maehr SA (1993). Core formation in the Moon: The mystery of the excess depletion of Mo, W and P. In *Lunar and Planetary Science Conference Proceedings*, vol. 24, pp. 1071–1072. bibcode:1993LPI....24.1071N

Newson HE (1995). Composition of the solar system, planets, meteorites, and major terrestrial reservoirs. In *Global Earth Physics: A Handbook of Physical Constants*, vol. 1. American Geophysical Union, Washington DC. doi:10.1029/RF001p0159

Nimmo F, Kleine T, Morbidelli A (2024). Tidally driven remelting around 4.35 billion years ago indicates the Moon is old. *Nature* 636(8043): 598–602. doi:10.1038/s41586-024-08231-0

O'Neill HSC (1991). The origin of the Moon and the early history of the Earth - a chemical model. Part 1: The Moon. *Geochimica et Cosmochimica Acta* 55: 1135–1157. doi:10.1016/0016-7037(91)90168-5

O'Neill HSC, Berry AJ, Eggins SM (2008). The solubility and oxidation state of tungsten in silicate melts: Implications for the comparative chemistry of W and Mo in planetary differentiation processes. *Chemical Geology* 255: 346–359. doi:10.1016/j.chemgeo.2008.07.005

O'Neill HSC, Eggins SM (2002). The effect of melt composition on trace element partitioning: An experimental investigation on the activity coefficients of FeO, NiO, CoO, MoO_2 and MoO_3. *Chemical Geology* 186: 151–181. doi:10.1016/S0009-2541(01)00414-4

Palme H, O'Neill H (2014). Cosmochemical Estimates of Mantle Composition. In Holland H, Turekian K (eds.) *Treatise on Geochemistry*, pp. 1–39. Elsevier, 2nd edn. doi:10.1016/B978-0-08-095975-7.00201-1

Palme H, Rammensee W (1982). The significance of W in planetary differentiation processes-Evidence from new data on eucrites. In *Lunar and Planetary Science Conference Proceedings*, vol. 12, pp. 949–964. bibcode:1982LPSC...12..949P

Palme H, Wänke H (1975). A unified trace-element model for the evolution of the lunar crust and mantle. In *Lunar and Planetary Science Conference Proceedings*, vol. 6, pp. 1179–1202. bibcode:1975LPSC....6.1179P

Rai N, Perrillat JP, Mezouar M, Colin A, Petitgirard S, Van Westrenen W (2019). In situ viscometry of primitive lunar magmas at high pressure and high temperature. *Frontiers in Earth Science* 7: 94. doi:10.3389/feart.2019.00094

Rai N, van Westrenen W (2014). Lunar core formation: new constraints from metal–silicate partitioning of siderophile elements. *Earth and Planetary Science Letters* 388: 343–352. doi:10.1016/j.epsl.2013.12.001

Righter K (2011). Prediction of metal–silicate partition coefficients for siderophile elements: An update and assessment of P-T conditions for metal–silicate equilibrium during accretion of the Earth. *Earth and Planetary Science Letters* 304(1-2): 158–167. doi:10.1016/j.epsl.2011.01.028

Rutherford MJ, Head JW, Saal AE, Hauri E, Wilson L (2017). Model for the origin, ascent, and eruption of lunar picritic magmas. *American Mineralogist* 102(10): 2045–2053. doi:10.2138/am-2017-5994ccbyncnd

Sato M (1978). Oxygen fugacity of basaltic magmas and the role of gas-forming elements. *Geophysical Research Letters* 5(6): 447–449. doi:10.1029/GL005i006p00447

Sharp M, Righter K, Walker RJ (2015). Estimation of trace element concentrations in the lunar magma ocean using mineral-and metal-silicate melt partition coefficients. *Meteoritics & Planetary Science* 50(4): 733–758. doi:10.1111/maps.12396

Shearer CK, Hess PC, Wieczorek MA, Pritchard ME, Parmentier EM, Borg LE, Longhi J, Elkins-Tanton LT, Neal CR, Antonenko I, Canup RM, Halliday AN, Grove TL, Hager BH, -C LD, Wiechert U (2006). Thermal and magmatic evolution of the Moon. *Reviews in Mineralogy and Geochemistry* 60(1): 365–518. doi:10.2138/rmg.2006.60.4

Simon SB, Sutton SR (2018). Valences of Ti, Cr, and V in Apollo 17 high-Ti and very low-Ti basalts and implications for their formation. *Meteoritics & Planetary Science* 53(10): 2138–2154. doi:10.1111/maps.13123

Smoliar MI, Walker RJ, Morgan JW (1996). Re-Os ages of group IIA, IIIA, IVA, and IVB iron meteorites. *Science* 271(5252): 1099. doi:10.1126/science.271.5252.1099

Snyder GA, Taylor LA, Neal CR (1992). A chemical model for generating the sources of mare basalts: Combined equilibrium and fractional crystallization of the lunar magmasphere. *Geochimica et Cosmochimica Acta* 56(10): 3809–3823. doi:10.1016/0016-7037(92)90172-F

Sprung P, Kleine T, Scherer EE (2013). Isotopic evidence for chondritic Lu/Hf and Sm/Nd of the Moon. *Earth and Planetary Science Letters* 380: 77–87. doi:10.1016/j.epsl.2013.08.018

Steele AM, Colson RO, Korotev RL, Haskin LA (1992). Apollo 15 green glass: Compositional distribution and petrogenesis. *Geochimica et Cosmochimica Acta* 56(11): 4075–4090. doi:10.1016/0016-7037(92)90017-D

Steenstra ES, Berndt J, Klemme S, Fei Y, van Westrenen W (2020). A possible high-temperature origin of the Moon and its geochemical consequences. *Earth and Planetary Science Letters* 538: 116222. doi:10.1016/j.epsl.2020.116222

Steenstra ES, Rai N, Knibbe JS, Lin YH, van Westrenen W (2016). New geochemical models of core formation in the Moon from metal–silicate partitioning of 15 siderophile elements. *Earth and Planetary Science Letters* 441: 1–9. doi:10.1016/j.epsl.2016.02.028

Steenstra ES, Seegers AX, Eising J, Tomassen BGJ, Webers FPF, Berndt J, Klemme S, Matveev S, van Westrenen W (2018). Evidence for a sulfur-undersaturated lunar interior from the solubility of sulfur in lunar melts and sulfide-silicate partitioning of siderophile elements. *Geochimica et Cosmochimica Acta* 231: 130–156. doi:10.1016/j.gca.2018.04.008

Steenstra ES, Sitabi AB, Lin YH, Rai N, Knibbe JS, Berndt J, Matveev S, van Westrenen W (2017). The effect of melt composition on metal-silicate partitioning of siderophile elements and constraints on core formation in the angrite parent body. *Geochimica et Cosmochimica Acta* 212: 62–83. doi:10.1016/j.gca.2017.05.034

Sutton SR, Jones KW, Gordon B, Rivers ML, Bajt S, Smith JV (1993). Reduced chromium in olivine grains from lunar basalt 15555: X-ray absorption near edge structure (XANES). *Geochimica et Cosmochimica Acta* 57(2): 461–468. doi:10.1016/0016-7037(93)90444-2

Takahashi E (1986). Melting of a dry peridotite KLB-1 up to 14 GPa: Implications on the origin of peridotitic upper mantle. *Journal of Geophysical Research: Solid Earth* 91(B9): 9367–9382. doi:10.1029/JB091iB09p09367

Taylor LA, Patchen A, Mayne RG, Taylor DH (2004). The most reduced rock from the Moon, Apollo 14 basalt 14053: Its unique features and their origin. *American Mineralogist* 89(11-12): 1617–1624. doi:10.2138/am-2004-11-1205

Terasaki H, Frost DJ, Rubie DC, Langenhorst F (2008). Percolative core formation in planetesimals. *Earth and Planetary Science Letters* 273(1-2): 132–137. doi:10.1016/j.epsl.2008.06.019

Thiemens MM, Sprung P, Fonseca ROC, Leitzke FP, Münker C (2019). Early Moon formation inferred from hafnium–tungsten systematics. *Nature Geoscience* 12(9): 696–700. doi:10.1038/s41561-019-0398-3

Wade J, Wood BJ, Tuff J (2012). Metal–silicate partitioning of Mo and W at high pressures and temperatures: evidence for late accretion of sulphur to the Earth. *Geochimica et Cosmochimica Acta* 85: 58–74. doi:10.1016/j.gca.2012.01.010

Wadhwa M (2008). Redox Conditions on Small Bodies, the Moon and Mars. *Reviews in Mineralogy and Geochemistry* 68: 493–510. doi:10.2138/rmg.2008.68.17

Weber RC, Lin PY, Garnero EJ, Williams Q, Lognonne P (2011). Seismic Detection of the Lunar Core. *Science* 331(6015): 309–312. doi:10.1126/science.1199375

Wetzel DT, Hauri EH, Saal AE, Rutherford MJ (2015). Carbon content and degassing history of the lunar volcanic glasses. *Nature Geoscience* 8(10): 755–758. doi:doi.org/10.1038/ngeo2511

Wohlgemuth-Ueberwasser C, Ballhaus C, Berndt J, Stotter née Paliulionyte V, Meisel T (2007). Synthesis of PGE sulfide standards for laser ablation inductively coupled plasma mass spectrometry (LA-ICP-MS). *Contributions to Mineralogy and Petrology* 154(5): 607–617. doi:10.1007/s00410-007-0212-x

Wolf R, Anders E (1980). Moon and Earth: compositional differences inferred from siderophiles, volatiles, and alkalis in basalts. *Geochimica et Cosmochimica Acta* 44(12): 2111–2124. doi:10.1016/0016-7037(80)90208-2

Wood BJ, Kiseeva ES, Mirolo FJ (2014). Accretion and core formation: the effects of sulfur on metal–silicate partition coefficients. *Geochimica et Cosmochimica Acta* 145: 248–267. doi:10.1016/j.gca.2014.09.002

Wood BJ, Wade J (2013). Activities and volatilities of trace components in silicate melts: a novel use of metal–silicate partitioning data. *Contributions to Mineralogy and Petrology* 166: 911–921. doi:10.1007/s00410-013-0896-z

Xia Y, Kiseeva ES, Wade J, Huang F (2019). The effect of core segregation on the Cu and Zn isotope composition of the silicate Moon. *Geochemical Perspectives Letters* 12: 12–17. doi:10.7185/geochemlet.1928

Yoshino T, Walter MJ, Katsura T (2003). Core formation in planetesimals triggered by permeable flow. *Nature* 422(6928): 154–157. doi:10.1038/nature01459

Zhang H, Yang W, Zhang D, Tian H, Ruan R, Hu S, Chen Y, Hui H, Lin Y, Mitchell RN, et al. (2024). Long-term reduced lunar mantle revealed by Chang'e-5 basalt. *Nature Communications* 15(1): 8328. doi:10.1038/s41467-024-52710-x

Zhang M, Li Y (2021). Breaking of Henry's law for sulfide liquid–basaltic melt partitioning of Pt and Pd. *Nature Communications* 12(1): 5994. doi:10.1038/s41467-021-26311-x